Lawrence Berkeley National Laboratory

Energy Geosciences

Title

A combined experimental and modelling study of granite hydrothermal alteration

Permalink

https://escholarship.org/uc/item/3nc3g2fm

Authors

Saldi, Giuseppe D
Knauss, Kevin G
Spycher, Nicolas
et al.

Publication Date

DOI

Copyright Information
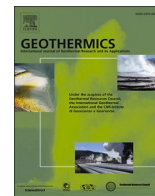
Miscellaneous geothermal topics

A combined experimental and modelling study of granite hydrothermal alteration

Giuseppe D. Saldi [a,*], Kevin G. Knauss [b], Nicolas Spycher [b], Eric H. Oelkers [c], Adrian P. Jones [d]

[a] *Géosciences Environnement Toulouse, GET-CNRS-CNES-IRD-OMP, Université de Toulouse, 14 ave. Edouard Belin, 31400 Toulouse, France*
[b] *Earth and Environmental Science Area, Lawrence Berkeley National Laboratory, 1 Cyclotron Road, MS74R316C, Berkeley (CA) 94720, USA*
[c] *Institute of Earth Sciences, University of Iceland, Sturlugata 7, Reykjavík 102, Iceland*
[d] *Earth Sciences Department, University College London, 5 Gower Place, London WC1E 6BS, UK*

ABSTRACT

Geochemical reactions can induce significant changes of rock reservoir porosity and permeability via mineral dissolution and precipitation processes, affecting the long-term fluid behaviour within various geological systems. The understanding and quantification of these reactions rely on field and experimental studies and on the predictions of reactive transport models.

The present study was aimed at assessing the extent to which current geochemical models integrating available mineral dissolution/precipitation rate equations can reproduce the experimental data obtained from 4 to 17-day long hydrothermal alteration experiments of a muscovite-biotite granite and, thus, help provide an accurate description of the evolution of geothermal systems within granitic reservoirs. The experiments were conducted at a constant temperature of 180 °C and over an aqueous fluid pH range of 2 to 8.5, using both mixed-flow and static batch reactors. Modelled major element (K, Al, Si, Ca, and Mg) concentrations were generally in satisfactory agreement with the corresponding measured elemental fluxes – the differences between modelled and experimental values were generally within a factor of 5 – and the predicted identity and mass of formed secondary phases were consistent with the microscopic observations of the reacted solids. However, larger differences between measured and modelled element concentrations were observed when significant amounts of secondary phases formed, notably at pH 2 to 3, and for longer-term batch experiments. Much of this concentration difference stems from the underestimation of the amounts of Al-phases formed at acid to near-neutral pH. Although an idealized rock composition was considered, the observed mismatch between model calculations and experimental data can be attributed to inadequate mineral precipitation reaction rates and a poor description of reactive surface areas in existing geochemical modelling codes. More accurate quantification of precipitation kinetics, including nucleation and growth, and improved descriptions of the temporal change of mineral surface area would enhance the predictive capabilities of reactive transport models and benefit, particularly, the efforts aimed at increasing the sustainability of EGS reservoirs.

1. Introduction

Most accessible geothermal energy resources around the world are hosted in volcanic and low permeability crystalline basement rocks, such as granitic bodies, where fluid circulation is limited or even absent (e.g., Duchane and Brown, 2002; Tester et al., 2006). In such systems, the development of enhanced geothermal systems (EGS) relies upon the generation of a network of permeable fractures by a combination of hydraulic fracturing and chemical stimulation procedures and their sustainability depends on the maintenance of an efficient fluid circulation through the fracture network (Entingh, 2000; Rose et al., 2007; Portier and Vuataz, 2010; Aqui and Zarrouk, 2011; Schill et al., 2017; Cheng et al., 2020).

Mass transfer driven by the interaction of circulating fluids with reservoir rocks can dramatically affect the evolution of the petrophysical properties, impacting the reservoir performance over time (e.g., Moore et al., 1994; Baldeyrou et al., 2003; Rosener and Géraud, 2015; Lo Ré et al., 2014; Sánchez-Roa et al., 2021), sometimes leading to mineral scales formation (cf. Reed, 1989; Stáhl et al., 2000; Gunnarson and Arnórsson, 2003; Xu et al., 2004; Nitschke et al., 2014). For this reason,

---

* Corresponding author.
  E-mail address: giuseppe.saldi@get.omp.eu (G.D. Saldi).
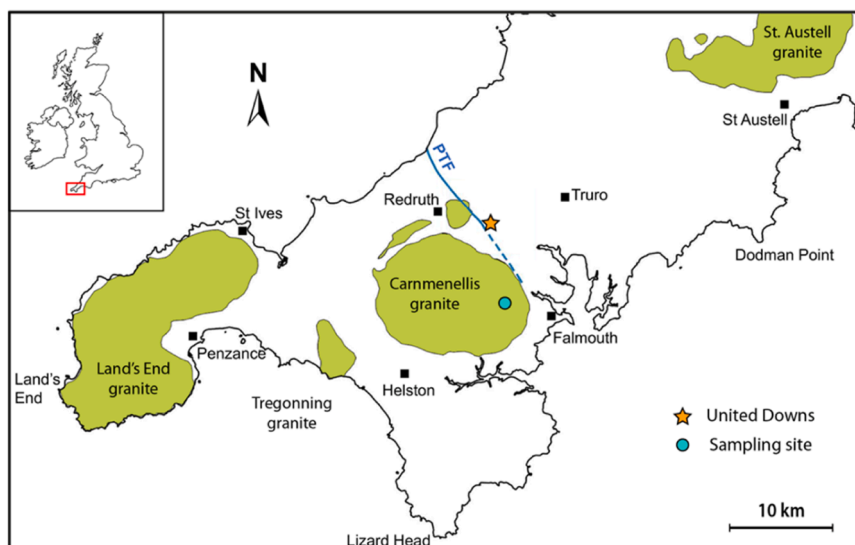
Fig. 1. Simplified map of South West Cornwall illustrating the main granite plutons of the Cornubian batholith, the location of the United Downs Deep Geothermal Power (UDDGP) project and the sampling site of the Carnmenellis granite used in this study. The approximate trace of the Porthtowan fault zone (PTF), through which the two directional wells of the UDDGP were drilled, is also drawn on the map (modified from Reinecker et al., 2021).

the quantification of hydrothermal alteration processes is key to assess the lifetime, economic viability as well as the environmental performance of EGS developed in these reservoirs (Lu, 2018; Paulillo et al., 2019).

The extent to which reservoir properties and fluid circulation are affected by geochemical reactions is commonly assessed by field tests and mineralogical studies, reactive transport models, and laboratory experiments conducted under relevant conditions (cf. Lu, 2018). Because of their high geothermal potential for EGS development, granitic rocks and high heat flow granite batholiths have been the targets of a great number of investigations over the past fifty years. The reactivity of these rocks was studied by analyses of the natural waters and the fluids produced during reservoir circulation tests performed at different geothermal sites (e.g., Edmunds et al., 1985; McCartney, 1987; Richards et al., 1992; Aquilina et al., 1997), whereas several experimental approaches and laboratory measurements and mineralogical analyses were adopted to characterize the alteration products and the physico-chemical changes induced by hydrothermal fluid-rock interaction (Charles, 1978; Bourg et al., 1985; Savage et al., 1987; Nishimoto and Yoshida, 2010; Sánchez-Roa et al., 2021) and by various thermo-mechanical and chemical treatments (Yashuara et al., 2011; Numakura et al., 2015; Watanabe et al., 2017; Meng et al., 2018; Farquharson et al., 2020; Schulz et al., 2022).

Several geochemical models of fluid-granite interaction have been developed to describe the sequence of alteration products observed in granite samples weathered naturally (Komminou and Yardley, 1997; Fritz et al., 2010; Ngo et al., 2016) or in the laboratory (e. g., Azaroual and Fouillac, 1997; Lo Ré et al., 2014). Different conceptual models and numerical simulations were also constructed to assess the impact of coupled thermal-hydraulic and chemical processes on the evolution of hosted geothermal systems (Bächler and Kohl, 2005; André et al., 2006; Pan et al., 2013; Lucas et al., 2020). The accurate temporal description of the alteration processes and evolution of reservoir properties requires the use of detailed dissolution/precipitation rate equations. The dissolution rates of rock forming minerals have been quantified by a large number of experimental studies and are reported by different reviews and kinetic data compilations (White and Brantley, 1995; Palandri and Kharaka, 2004; Marini, 2006; Bandstra et al., 2008; Heřmanská et al., 2022). The application of single mineral rate laws to the description of a multi-mineral system, however, presents several challenges because of the intrinsic and extrinsic factors that affect natural settings (cf. Velbel,

1993; White and Brantley, 2003; Ganor et al., 2005; Maher, 2010; White et al., 2017), particularly the formation of secondary phases and mineral coatings that could slow the dissolution of primary minerals. Such effects are generally poorly constrained and not adequately taken into account by reactive transport models (cf. Ganor et al., 2007; Goddéris et al., 2006; Maher et al., 2009; Aradóttir et al., 2015; Wild et al., 2016; Daval et al., 2018). In addition, the extent to which different sets of rate equations are able to match the dissolution rates of multi-mineral rocks under well-defined conditions has not been extensively evaluated and should be considered by combined experimental and modelling studies.

Although the elemental release rates of a multi-mineral rock can reflect, in some cases, the dissolution rates of individual mineral constituents (e.g., Critelli et al., 2014), this assumption may not be applicable under hydrothermal conditions, to rocks that underwent a significant degree of alteration and for long time periods (cf. White and Brantley, 2003; White et al., 2017). Ganor et al. (2005), for instance, who reacted both an altered granite and mineral-rich fractions separated from the same rock at pH 1 and 25 °C, reported slower dissolution rates for plagioclase and different dissolution behaviour of chlorite/biotite in the bulk granite compared to the corresponding mineral-rich fractions. The slower plagioclase dissolution in the granite was attributed to the presence of a Fe-rich coating and concomitant biotite dissolution, whereas the dissolution of biotite and chlorite were found to be affected by the precipitation of secondary phases, different fluid composition evolution and the alternation of wetting and drying cycles. Several experimental studies investigated the relative dissolution behaviour and rates of granite mineral constituents from bulk rock elemental release data (Afifi et al., 1985; Ganor et al., 2005; Wu et al., 2008; Takaya, 2014; White et al., 2017; Schulz et al., 2022) but most of these works were either limited to low temperature conditions or to a narrow range of pH and fluid chemical compositions, and they often provided only a qualitative analysis of the relative rates of reaction.

The revival of deep geothermal energy exploration in Cornwall (UK), where two deep wells were drilled through the Carnmenellis granite pluton for heat and power generation (Reinecker et al., 2021), provided the opportunity to investigate experimentally the reactivity of this geothermal reservoir rock at the expected subsurface temperature of 180 °C. The experimental results have been used to assess the capability of commonly used rate laws of mineral dissolution/precipitation to reproduce the geochemical evolution of the system. The purpose of this communication is to present the results of this combined experimental

Table 1
Chemical composition of the Carnmenellis granite sample used for the experimental study.

Oxide/ Element	Wt%	Element	Concentration ppm
SiO_2	72.76	Ba	290
Al_2O_3	14.45	Be	6
Fe_2O_3	1.7	Cr	9
MnO	0.04	Cs	16.4
MgO	0.52	Pb	38
CaO	1.02	Rb	240
Na_2O	2.62	Sr	126
K_2O	5.28	U	16.4
TiO_2	0.24	Th	16.8
P_2O_5	0.22	V	13
CO_2	0.24	Zn	67
F	0.11	Zr	203
Li	0.02	B	184
LOI	1.51	Y	7

Table 2
List of the mineral phases found in the Carnmenellis granite with the corresponding chemical formula as determined by electron microprobe analyses.

Mineral phase	Chemical formula
K-feldspar	$K_{0.85}Na_{0.13}Al_{1.01}Si_{3.0}O_8$
Albite	$Na_{0.90}K_{0.02}Ca_{0.10}Al_{1.09}Si_{2.90}O_8$
Biotite	$K_{0.83}Na_{0.02}(Fe_{1.27}Mg_{0.57}Ti_{0.14}Mn_{0.02})Al_{1.62}Si_{2.51}O_{10}(OH,F)_2$
Muscovite	$K_{0.79}Na_{0.07}Mg_{0.08}Fe_{0.08}Ti_{0.02}Al_{2.50}Si_{2.80}O_{10}(OH,F)_2$
Ilmenite	$Fe_{0.88}Mn_{0.11}Ti_{1.00}O_3$
Quartz	SiO_2

and geochemical modelling study and to use these results to identify the critical physical and chemical parameters most lacking for the accurate modelling of these water-rock systems.

2. Materials and methods

2.1. Solid sample preparation and characterization

The granite powder used for the experimental study was obtained from a homogeneous block of medium-grained porphyritic Carnmenellis granite from the Trenoweth Quarry, located 2 km SW of Penryn and ~9 km south of the United Downs Deep Geothermal Power (UDDGP) project site in Cornwall (UK). A schematic map of the UDDGP site and the sampling locations is shown in Fig. 1. The granite sample was initially broken with a hammer to mm-sized pieces, ground in an agate mortar and pestle and then sieved to obtain a 100–200 μm size fraction. The rock powder thus obtained was washed in ultrapure deionized water (18.2 MΩ·cm) and ultrasonically cleaned in ethanol to eliminate the fine particles from the surface of the generated mineral grains. This process was repeated several times until the supernatant became clear. After the cleaning procedure the granite powder was dried in an oven at 60 °C.

The chemical and mineralogical characterization of the granite sample was accomplished by bulk chemical analyses, electron microprobe analyses (EMPA, Cameca SXFive) of the original granite block and X-ray diffraction (XRD) analyses of the 100–200 μm powder used in the experiments. The chemical analyses of the Carnmenellis granite were conducted by the Activation Laboratories Ltd. (Ancaster, ON, Canada). Total oxide and metal concentrations were obtained by instrumental neutron activation analyses (INAA) and ICP-OES and ICP-MS analyses after total acid digestion of the rock sample. The measured chemical composition of the rock is summarized in Table 1. The average chemical compositions of single mineral phases were determined by EMPA on thin sections of this rock sample and are reported in Table 2. Note that the redox state of Fe in the micas was not determined but can be mostly considered as Fe(II), in agreement with biotite analyses of the same

Table 3
Relative abundances of Carnmenellis granite minerals determined by Rietveld refinement of the X-ray diffraction data and by normative calculations based on the chemical analyses reported in Table 1.

Mineral	Wt% (XRD)	Wt% (normative)
Quartz	36.23 ± 0.26	36.7
Albite	21.99 ± 0.28	22.8
Microcline	25.32 ± 0.29	19.8
Muscovite	7.71 ± 0.23	14.8
Biotite	3.03 ± 0.17	5.0
Montmorillonite-Ca	3.76 ± 0.20	n.d.
Chlorite	1.02 ± 0.12	n.d.
Ilmenite	0.335 ± 0.053	0.1
Fluorapatite	0.595 ± 0.095	1.1
Total	100.00	100.4

granite reported by Edmunds et al. (1985).

The relative abundance of the mineral phases identified in the rock sample used for the experimental work was determined by Rietveld refinement of the corresponding XRD pattern and is reported in Table 3.

The fresh granite powder was also characterized by scanning electron microscopy (FEG-SEM, JEOL JSM 7800F) coupled with energy dispersive X-ray (EDX) spectroscopy to observe the shape and surface features of the mineral grains and obtain insights into the structural relationships amongst the various mineral phases within the size fraction prepared for the experiments. SEM observations (Fig. 2) allowed identification of the main mineral components and showed that most of the grains were comprised of single mineral phases, except for the minor constituents.

The specific surface area (SSA) of the fresh granite mineral powder was measured by 11-point Kr adsorption analyses according to the BET method (SSA_{BET}) and was found to be equal to 0.4344 ± 5% m²/g. The contribution of each mineral phase to the total SSA of the solid was assessed by calculating the geometric specific surface area (SSA_{geo}) for each mineral using the following expression (cf. Tester et al., 1994; Gautier et al., 2001):

$$SSA_{geo} = \frac{6}{\rho \cdot d_e}, \tag{1}$$

where ρ is the density of the mineral and d_e represents the effective diameter of the mineral grains for a homogeneous particle distribution, such that (Tester et al., 1994):

$$d_e = \frac{d_{max} - d_{min}}{\ln\left(\frac{d_{max}}{d_{min}}\right)}, \tag{2}$$

where d_{max} and d_{min} stand for, respectively, the maximum and minimum particle sizes obtained by sieving. Eqs. (1) and (2) approximate the mineral grains to spherical particles with smooth surfaces but cannot adequately express the surface area of micas and other sheet silicates due to their distinct shape. For these minerals the following expression was adopted to calculate the geometric surface area (cf. Macht et al., 2011):

$$SSA_{geo} = \frac{2D + 4h}{\rho \cdot D \cdot h}, \tag{3}$$

where D is the particle horizontal dimension and h represents its thickness along the third dimension. For the sheet silicates identified by analyses of the granite sample D was assumed to coincide with d_e, whereas h was estimated based on SEM observations of the mineral powder for biotite and muscovite. For the sheet silicates that could not be clearly identified by EMPA and SEM analyses, namely chlorite and smectite, the geometric SSA was fixed via calibration modelling of the experimental results (see Section 2.3 below). The list of the starting SSA_{geo} values determined for each mineral is reported in Table 4.
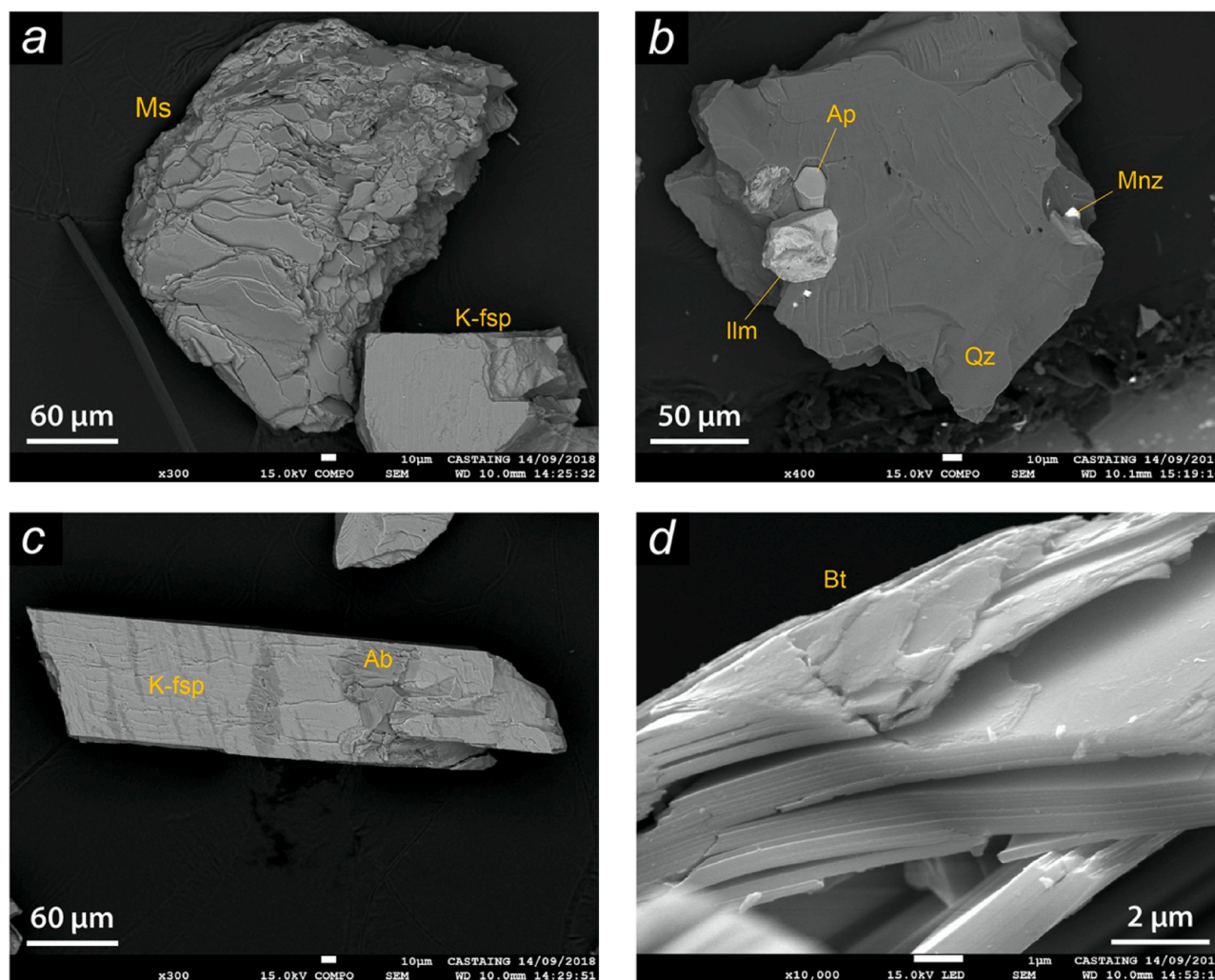
Fig. 2. SEM microphotographs of the granite powder (100–200 μm) prepared for the hydrothermal experiments showing the main mineral components with some accessory phases: (a) muscovite and K-feldspar grains; (b) back-scattered image of a quartz grain with included apatite, ilmenite and traces of monazite (REE-phosphate); (c) example of perthite, intergrown K-feldspar (bright areas) and albite (darker areas); (d) detail of a biotite grain with exposed individual sheets.

Table 4
Summary of the specific surface areas of the granite minerals identified in the powder used for the experiments based on the assumed geometry of the corresponding mineral grains (see text for details).

Mineral	SSA_{geo} cm^2/g
Quartz	156.9
Albite	158.7
Orthoclase	162.4
Muscovite	334.7
Biotite	305.5
Montmorillonite-Ca	1820.1[†]
Chlorite	1614.1[†]
Apatite	132.0
Ilmenite	231.1

[†] Values initially attributed by geochemical modelling calculations.

Considering the relative abundance of each mineral, as determined by XRD analyses, the initially estimated SSA_{geo} of the granite powder used in this study is equal to 0.0252 m^2/g, which is 17 times lower than the specific surface area measured by the BET method (0.4344 m^2/g).

2.2. Experiments and fluid chemical analyses

The hydrothermal alteration of Carnmenellis granite was studied using two distinct experimental approaches: 1) using mixed-flow reactor experiments (MFR) and 2) under static conditions, using batch reactor experiments (SBR). All experiments were conducted at 180 °C in an aqueous solutions of 0.01 M NaCl, with additions of HCl, NaOH and B(OH)$_3$ to adjust the fluid pH to the desired value, with the exception of one experiment carried out at pH 2 consisting of a solution of 0.01 M HCl. This temperature is within the 175–190 °C range of values expected for the circulating fluids at the United Downs geothermal system (Reinecker et al., 2021).

The mixed-flow reactor (MFR) experiments were conducted using a 300 ml Parr Ti-reactor, modified to work at constant fluid flow conditions. All the parts of the reactor in contact with the fluid phase were made of commercially pure titanium. The reactive fluid was delivered to the MFR by a Gilson 307 HPLC piston pump while the pressure through the system was held at 18 bar by a back pressure regulator. Flow rates were of 0.4–0.5 g/min and the amount of solid used for each experiment was 3.0–3.5 g. The reactor temperature was maintained at 180 ± 2 °C by a Parr-controlled furnace and the fluid inside the reactor vessel was continuously stirred at a rate of ~ 150 rpm. The outlet fluid was filtered through a ~10 μm Ti-frit fixed at the bottom of the dip-tube inside the reaction vessel and cooled to ambient temperature as it left the reactor

Table 5

Summary of the hydrothermal conditions of the mixed-flow rector (MFR) and static batch reactor (SBR) experiments conducted in the present study.

	Experiment #	pH (20 °C)	NaCl mM	HCl mM	NaOH mM	B(OH)₃ mM	Solid g	FFR[‡] g/min	Duration days
MFR	CW1[*]	3.99	10	0.1	–	–	3.514	0.4	5.9
	CW2[*]	2.98	10	1	–	–	3.510	0.5	4.1
	CW3	9.02	10	–	0.96	2.5	3.505	0.4	6.0
	CW5	10.55	8.25	–	2.72	2.5	3.506	0.4	5.7
	CW7	2.02	–	10	–	–	3.005	0.4	6.2
SBR	CWA	4.03	10	0.1	–	–	4.573	n.a.	16.7
	CWB	10.66	8.25	–	2.72	2.5	3.018	n.a.	15.1

[*] Initially filled with deionized water.
[‡] Fluid flow rate.
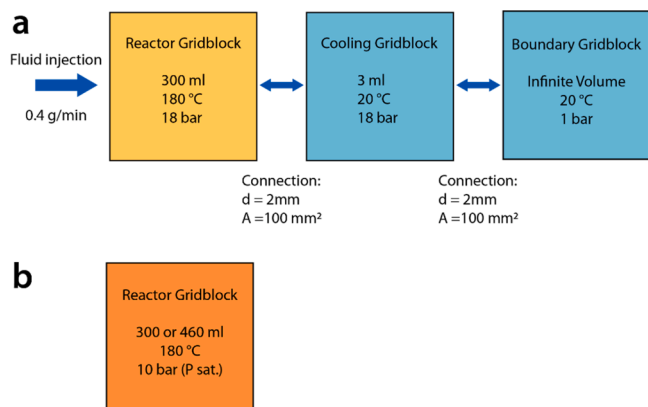
Fig. 3. Conceptual model of the two reactors used in this study, adopted to simulate the results of the experiments: (a) mixed-flow reactor (MFR); (b) static batch reactor (SBR).

Table 6

Idealized mineral composition and properties of primary and potential secondary phases used in the conceptual models to simulate the experimental results.

Mineral	Weight%	Volume fraction	A_{min} m^2_{min}/m^3_{min}
Quartz	36.23	0.3638	4.16e+4
Albite	19.79	0.2012	4.16e+4
Anorthite	2.20	0.0225	1.20e+4
Max. microcline	25.32	0.2631	2.00e+6
Muscovite	7.71	0.0724	9.44e+4
Annite	3.03	0.0243	9.44e+4
Montmorillonite-Ca	3.76	0.0356	4.28e+5
Clinochlore-14A	1.02	0.0101	1.07e+4
Ilmenite	0.335	0.0019	4.16e+4
Fluorapatite	0.595	0.0050	4.16e+4
Kaolinite	0	0	4.28e+5
Gibbsite	0	0	4.28e+5
Bohemite	0	0	4.28e+5
Illite	0	0	4.28e+5
Montmorillonite-K	0	0	4.28e+5

using a cooling sleeve installed along the outlet fluid line. The duration of these experiments varied between 4 and 6 days. The experimental conditions of these experiments are listed in Table 5.

Two batch experiments were conducted using 460 and 300 ml Parr Ti-reactors to study the alteration of the same granite sample at mildly acidic (initial pH = 4.0) and basic conditions (initial pH = 10.7). A summary of these experimental conditions is presented in Table 5. A nitrogen pressure of 25 to 40 bar was applied to the head space of the reactor to keep the reactive fluid in the liquid state. The fluid samples withdrawn from the reactor were filtered via a Ti-frit and cooled to room temperature using a cooling sleeve located along the fluid line before the sampling valve. Fluid samples were regularly collected as a function of time, filtered using a 0.20 μm syringe filter, acidified with concentrated ultrapure HNO_3 and stored in a fridge before chemical analyses.

The fluid samples collected during the experiments were analysed for the major elements (Si, K, Al, Ca, Mg, Na, and Fe) by ICP-OES and for a number of relevant dissolved trace elements (Li, Ti, Cr, Mn, Fe, Ni, Rb, Sr, Ba, B, Mo, Cu and Zn) by ICP-MS. The uncertainty of the analytical data was generally lower than 2%. pH measurements of the aqueous samples were made at 20 °C immediately after sampling using a Metrohm pH microelectrode previously calibrated against NIST certified buffer solutions. Measured pH values were successively recomputed at 180 °C using the code EQ3/6 (Wolery, 2010) with the database *data0. ymp. R5* (Wolery and Jarek, 2003; Wolery and Jové Colón, 2017)

2.3. Geochemical modelling

To aid in interpreting the experimental results of this study we employed conceptual models of the two types of reactors used in the laboratory: MFR and SBR. The conceptual model of the MFR is illustrated in Fig. 3a. In this model at time $t = 0$ the Reactor Gridblock is either filled initially with distilled water (expts. CW1 and CW2) or with

the incoming injected fluid (CW3, CW5, CW7; see Table 5) in order to replicate the exact experimental conditions in each case. The Reactor Gridblock also contains the Cornwall granite to be reacted. Following initial computation of the fluid speciation at 20 °C and time $t = 0$, the fluid temperature is instantaneously raised to 180 °C and speciation recomputed at this temperature; then kinetically-controlled chemical reaction between the fluid and the solid is simulated as the injected fluid begins flowing. The Boundary Gridblock is assumed to have infinite volume, so that during the simulation there is no pressure buildup in the system. The Cooling Gridblock represents the small dead volume between the MFR and the Back Pressure Regulator present in the physical experimental apparatus, and in which there are no minerals initially present, and no minerals are allowed to precipitate. Within the Cooling Gridblock, the fluid exiting the MFR is instantaneously cooled to 20 °C and the speciation of the aqueous fluid is re-computed in the absence of minerals, and with no minerals allowed to precipitate as a result of the temperature drop, thus representing the fluid sample collected for analyses.

The conceptual model for the SBR (Fig. 3b) is a single box of either 300 or 460 ml. In this model at $t = 0$ the reactor is filled with the reacting fluid and contains the powdered Cornwall granite to be reacted. Following initial 20 °C speciation of the fluid at $t = 0$, the fluid temperature is instantaneously raised to 180 °C. The fluid speciation is then re-computed, followed by the simulation of kinetically-controlled chemical reaction of the fluid with the solid. The fluid pressure is assumed to equal the fluid saturation pressure at the reaction temperature (180 °C). Because this is a static (closed) system, at each sample point in time the model simulates the (essentially) instantaneous extraction of an amount of fluid equivalent to the experimental sample size, recalculates the liquid/solid ratio ("porosity"), and then proceeds with simulating the reaction of the remaining reacted fluid and solid following the sample withdrawal.

Table 7

Summary of the rate equation parameters used to model the rates of fluid-granite interaction. The listed parameters refer to Eq. (5) and are taken from Palandri and Kharaka (2004).

Mineral	Acid mechanism			Neutral mechanism		Base mechanism		
	$\log k$[a]	E[b]	n	$\log k$	E	$\log k$	E	n
Quartz	–	–	–	−13.34	90.1	–	–	–
Albite	−10.16	65.0	0.457	−12.56	69.8	−15.6	71.0	−0.572
Anorthite	−3.50	16.6	1.411	−9.12	17.8	−12.16	17.8	−0.572
Max. Microcline	−10.06	51.7	0.500	−12.41	38.0	−21.20	94.1	−0.823
Muscovite	−11.85	22.0	0.370	−13.55	22.0	−14.55	22.0	−0.220
Annite[c]	−11.85	22.0	0.370	−13.55	22.0	−13.55	22.0	−0.220
Montmorillonite-Ca[d]	−12.71	48.0	0.220	−14.41	48.0	−14.41	48.0	−0.130
Clinochlore-14A	−11.11	88.0	0.500	−12.52	88.0	–	–	–
Ilmenite	−8.35	37.9	0.421	−11.16	37.9	–	–	–
Fluorapatite	−3.73	250.0	0.613	−8.00	250.0	–	–	–
Kaolinite	−11.31	65.9	0.777	−13.18	22.2	−17.05	17.9	−0.472
Gibbsite	−7.65	47.5	0.992	−11.50	61.2	−16.65	80.1	−0.784
Boehmite[e]	−7.65	47.5	0.992	−11.50	61.2	−16.65	80.1	−0.784
Illite[f]	−11.85	22.0	0.370	−13.55	22.0	−14.55	22.0	−0.220
Montmorillonite-K	−12.71	48.0	0.220	−14.41	48.0	−14.41	48.0	−0.130

[a] = rate constant in mol m^{-2} s^{-1}.

[b] = activation energy in kJ/mol.

[c] = assume equal to Muscovite, except base rate is 10× faster.

[d] = assume equal to the Montmorillonite-K in Palandri and Kharaka (2004).

[e] = assume equal to Gibbsite.

[f] = assume equal to Muscovite.

We used the TOUGHREACT reactive transport simulator (Xu et al., 2011) developed at LBNL (in-house upgrade of version 3.32) to model the experiments, based on the two conceptual models described above, together with the equation of state module EOS1. The thermodynamic data file used (*tk2-ympR5-HS.dat*) was derived directly from the EQ3/6 database *data0.ymp.R5*. The rock properties of the primary and potential secondary minerals, as identified using XRD and EMP analyses, for the Cornwall granite used in the calculations are provided in Table 6. For this purpose we have converted the weight-based SSA$_{geo}$ for each mineral to the volume-based A$_{min}$, by multiplying them by their respective mineral densities. Note that an idealized rock composition was required for the geochemical model to adapt the mineralogical composition of the rock to the kinetic parameters existing in the literature. Note also that the available rate equations refer either to pure mineral phases or equivalent phases with different chemical composition.

Rate equations derived from transition state theory (Lasaga, 1998) were used in the simulations, with the reaction rate r defined as:

$$r = k[1 - (Q/K)^m]$$ (4)

with Q/K representing the mineral saturation index (ion activity product Q divided by the equilibrium constant K), and m being an exponent related to the Temkin coefficient. The value of m adopted in this study is equal to the inverse of the number of silica atoms in the mineral formula for silicates, and equal to unity for other minerals. The rate constant k was implemented with multiple mechanisms (acid, neutral, and alkaline) as described in Xu et al. (2011) and Palandri and Kharaka (2004) using:

$$k = k_{25}^{nu}\exp\left[\frac{-E_a^{nu}}{R}\left(\frac{1}{T} - \frac{1}{298.15}\right)\right] + k_{25}^{H}\exp\left[\frac{-E_a^{H}}{R}\left(\frac{1}{T} - \frac{1}{298.15}\right)\right]a_H^{n_H}$$
$$+ k_{25}^{OH}\exp\left[\frac{-E_a^{OH}}{R}\left(\frac{1}{T} - \frac{1}{298.15}\right)\right]a_{OH}^{n_{OH}}$$ (5)

where E_a represents the activation energy; R is the Gas Constant; T is the temperature of interest; superscripts or subscripts nu, H, and OH indicate neutral, acid and base mechanisms, respectively; a is the activity of the i aqueous species; and n denotes the reaction order. This 3-term equation accounts for separate mechanisms for each pH region (acid, neutral and base). The rate law data used in the simulations are provided in Table 7. For consistency these are taken directly from Palandri and Kharaka (2004).

In the simulations some general assumptions were made about mineral growth based on their observed behaviour in the experiments and in nature. We assumed that in the reactor quartz, anorthite, clinochlore, ilmenite and fluorapatite would only dissolve and not grow. The other primary minerals in the Cornwall granite (albite, microcline, muscovite, annite, and montmorillonite-Ca) would be allowed to grow, if they should become supersaturated in the reactor fluid, as would the potential secondary minerals (kaolinite, gibbsite, boehmite, illite and montmorillomite-K). For all the secondary minerals with respect to which the fluid became supersaturated in the simulation, an initial volume fraction of 1.0×10^{-5} and initial particle radius of 1.0×10^{-8} m were assumed, irrespective of the initial fluid composition. These two parameters are used by TOUGHREACT to approximate the nucleation of secondary phases not initially present. As these secondary minerals grow, the number of mineral grains decreases while their radius increases so that the corresponding surface area decreases to reach the input value for the mineral (see A$_{min}$ values in Table 6). We assumed that in the MFR Cooling Gridblock no minerals would grow, regardless of their saturation state. We assumed that the precautions taken during preparation of the vessel filling and injected fluids were sufficient to preclude saturation with respect to atmospheric gases, e.g., CO$_2$. The dissolved amount of this gas contributed from atmosphere was, therefore, considered as negligible and not included in the chemical description of the aqueous solutions. We also assumed that the reactions were redox insensitive and the valence state of each element remained that of its basis species. This implies that dissolved iron kept the reduced state of the defined basis species (Fe^{2+}) in all the modelling calculations. Note that the Fe-bearing phases defined in our system (annite and ilmenite) contain only Fe^{2+} in their chemical formula, so that their dissolution does not involve any valence state change. This assumption, however, does not allow describing the formation, although limited, of secondary Fe(III)-oxides observed in one experiment.

Using experiment CW3, we loosely calibrated the specific surface areas of microcline (×50), chlorite (/40) and anorthite (/3.5) to best match the experimental results. Note that the starting model mineral surface areas were based on simplistic geometric calculations assuming idealized form, neglecting surface roughness and internal porosity. No alteration was made to any other thermodynamic or kinetic properties from the aforementioned sources.

The simulations done for the remaining experiments (CW1, CW2, CW5, CW7, CWA and CWB) were all made using the same set of input

a. Experimental data and model results of Expt. CW1
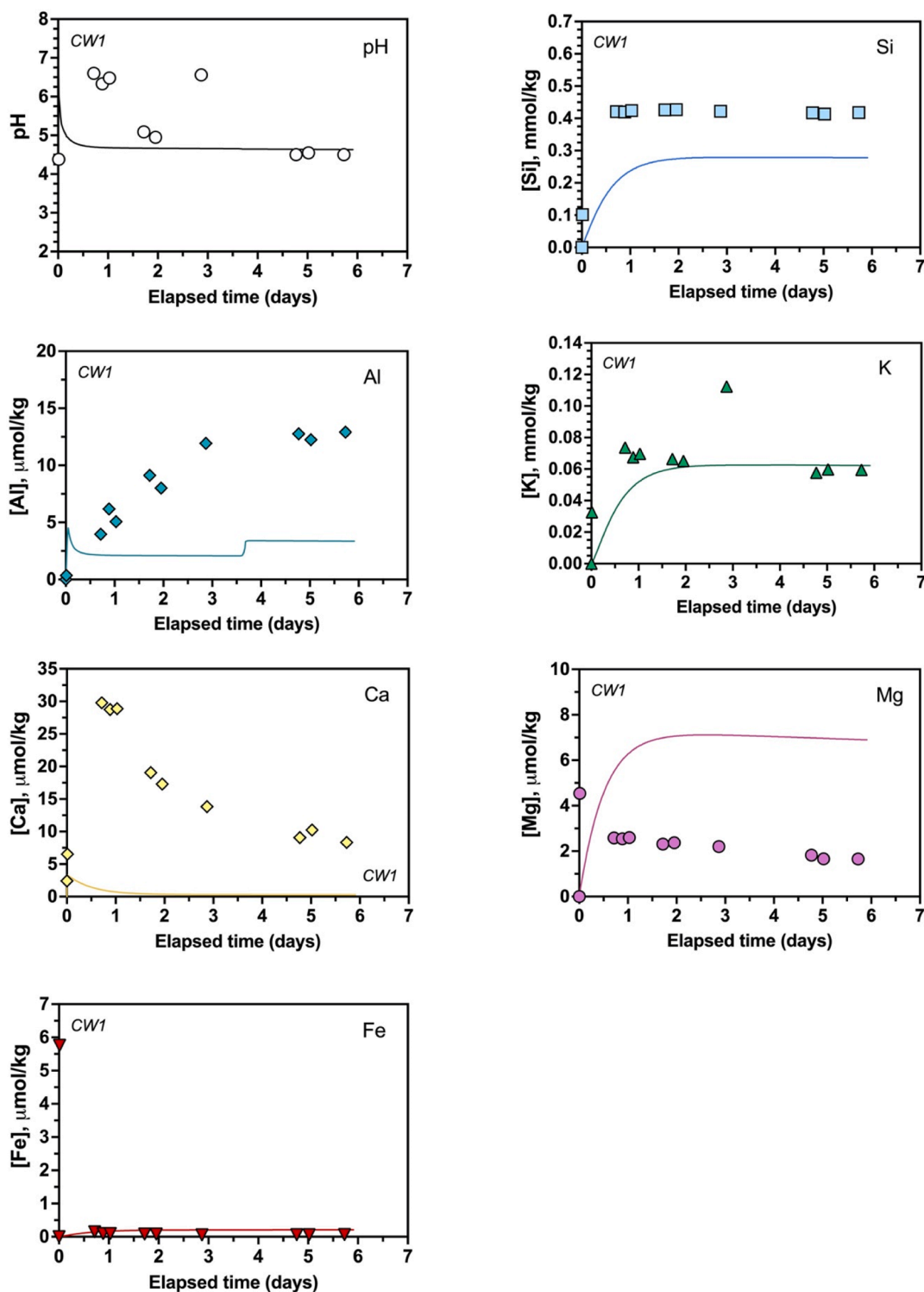
Fig. 4. Comparison between the evolution of reactive fluid concentrations measured during the dissolution experiments conducted with mixed-flow reactors (coloured symbols) and those calculated by the kinetic models (continuous lines). All experiments were carried out at a constant temperature of 180 ± 2 °C and constant ionic strength ($I = 0.01$ M). Note that, although the measured concentrations refer to samples collected at ambient temperature, no further reaction is assumed to take place in the model after the fluid leaves the reactor and is cooled. The uncertainties of measured element concentration are smaller than the size of the symbols. The experimental pH values at 180 °C were recalculated from the measurements at 20 °C using the EQ3/6 code (Wolery, 2010). (a) Experiment CW1: initial fluid pH (20 °C) = 3.99; (b) experiment CW2: pH (20 °C) = 2.98; (c) experiment CW3: pH (20 °C) = 9.02; (d) experiment CW5: pH (20 °C) = 10.55; (e) experiment CW7: pH (20 °C) = 2.02.

b. Experimental data and model results of Expt. CW2
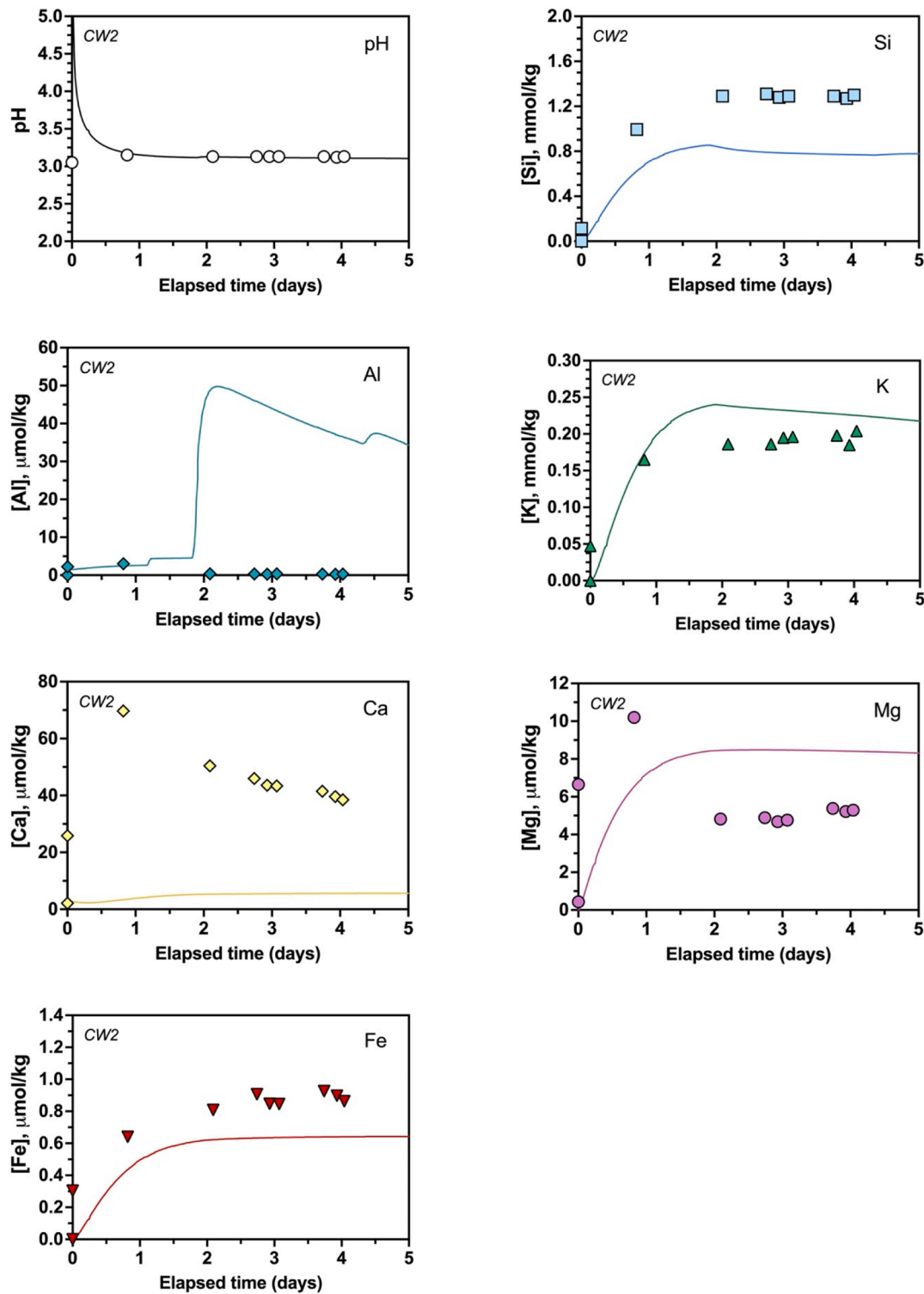
Fig. 4. (*continued*).

parameters that resulted from the fitting of the CW3 results. Note that the simulations include both flowing, open system experiments, and closed system experiments with evolving surface area/fluid volume conditions and spanning a 20 °C pH range from 3 to nearly 11. Model fit to the experimental results for these remaining experiments was generally good but, as expected, variable and not quite as "good" as the

CW3 calibration.

To improve the match between simulated and experimental results, we explored a number of other modelling options as follows, although none of these were successful and thus none of these were pursued further. First, we assumed that in spite of efforts made to exclude equilibration of the initial fluids with atmospheric CO_2, they were, in

c. Experimental data and model results of Expt. CW3
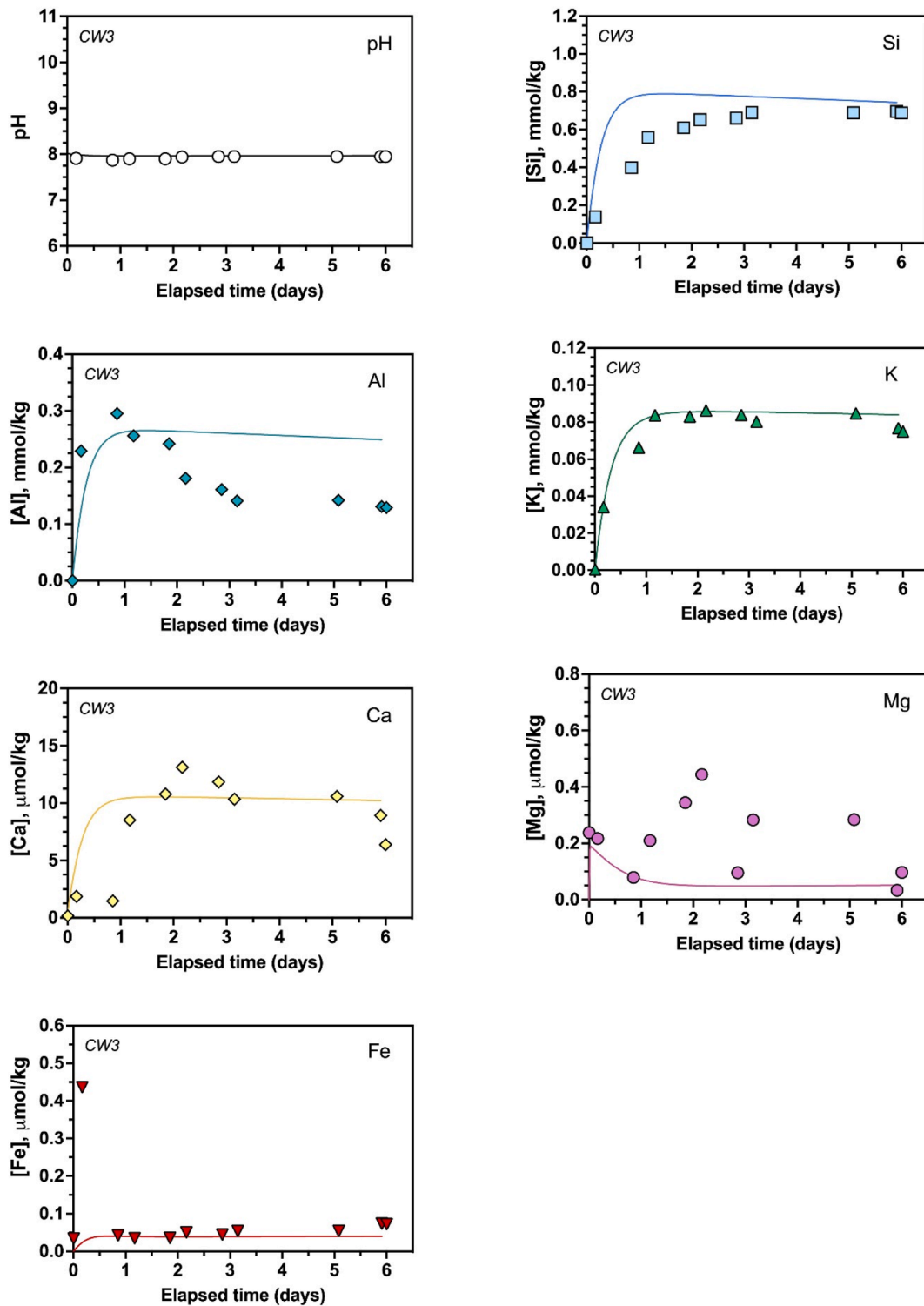
Fig. 4. (*continued*).

fact, saturated with respect to this gas and contained the corresponding amount of dissolved CO_2 species. We also then added the appropriate carbonate minerals to the suite of potential secondary minerals. This did not improve the fit, likely due to the fact that the fluids never became supersaturated with respect to the carbonate minerals given the relatively small amount of CO_2 added to the initial fluids as a result of

atmospheric gas equilibration. Second, we explored adding ion exchange to the simulation by assuming that the starting rock contained a generic Na^+ ion exchanger with cation exchange capacity (CEC) = 40 meq/100 g solid. As described by Appelo (1994), we used commonly observed freshwater exchange coefficient values ($Na^+ = 1$, $K^+ = 0.2$, $Mg^{2+} = 0.5$, $Ca^{2+} = 0.4$, and H^+ set by trial and error). Note that these

d.   *Experimental data and model results of Expt. CW5*
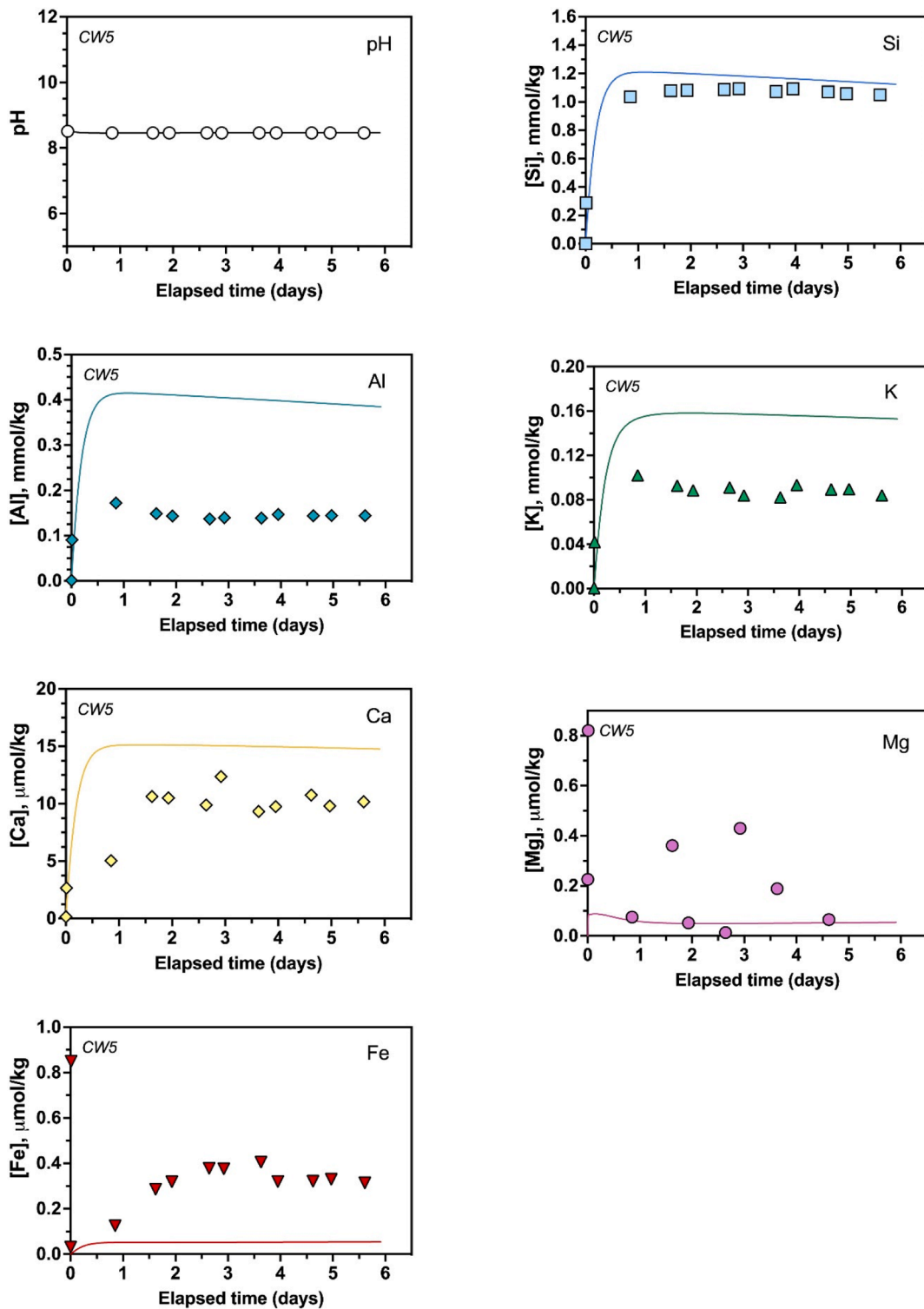
Fig. 4. (continued).

values are for 25 °C. While this did improve the fit of the alkalis and alkaline earths for CW1, for example, applying the same exchange co-efficient values to CW2 (and other experiments) resulted in worse fit than not including ion exchange at all. Third, we tried arbitrarily altering some of the rate equation parameters (rate constants, catalysing species exponents, etc.) from Palandri and Kharaka (2004) for specific

minerals (anorthite, kaolinite, etc.) to improve the fit of the measured concentrations, again using CW1 as the test case. As with the ion ex-change effort, in some cases this improved the CW1 fit, but it resulted in worse fit for other experiments and was, by definition, completely arbitrary.

e. *Experimental data and model results of Expt. CW7*
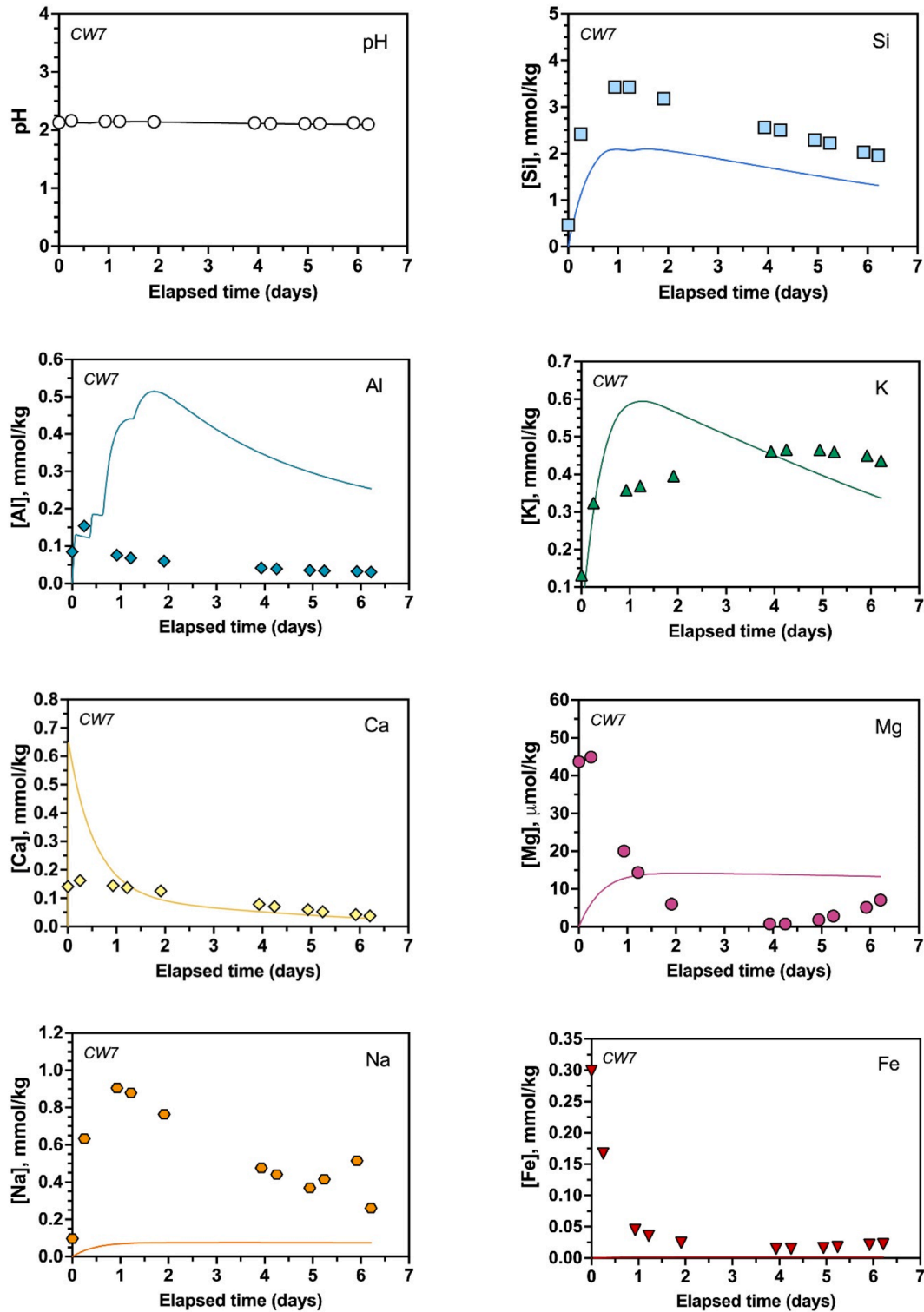
Fig. 4. (*continued*).

3. Experimental results

The chemical compositions of the fluids interacting with the granite during the MFR and SBR experiments are illustrated in Figs. 4 and 5, respectively, and summarized by the Tables in Appendices A and B. Note that trace element concentrations from the MFR experiments are generally very low or below the detection limit for ICP-MS and, there-fore, were not reported on the plots. Note also that, for the elements presented by the plots, the uncertainties of the measured concentrations are comprised within the symbol size. The illustrated pH values corre-spond to the pH of the fluid samples calculated at 180 °C from the measurements made at 20 °C. These calculations were performed using

a. Experimental data and model results of Expt. CWA
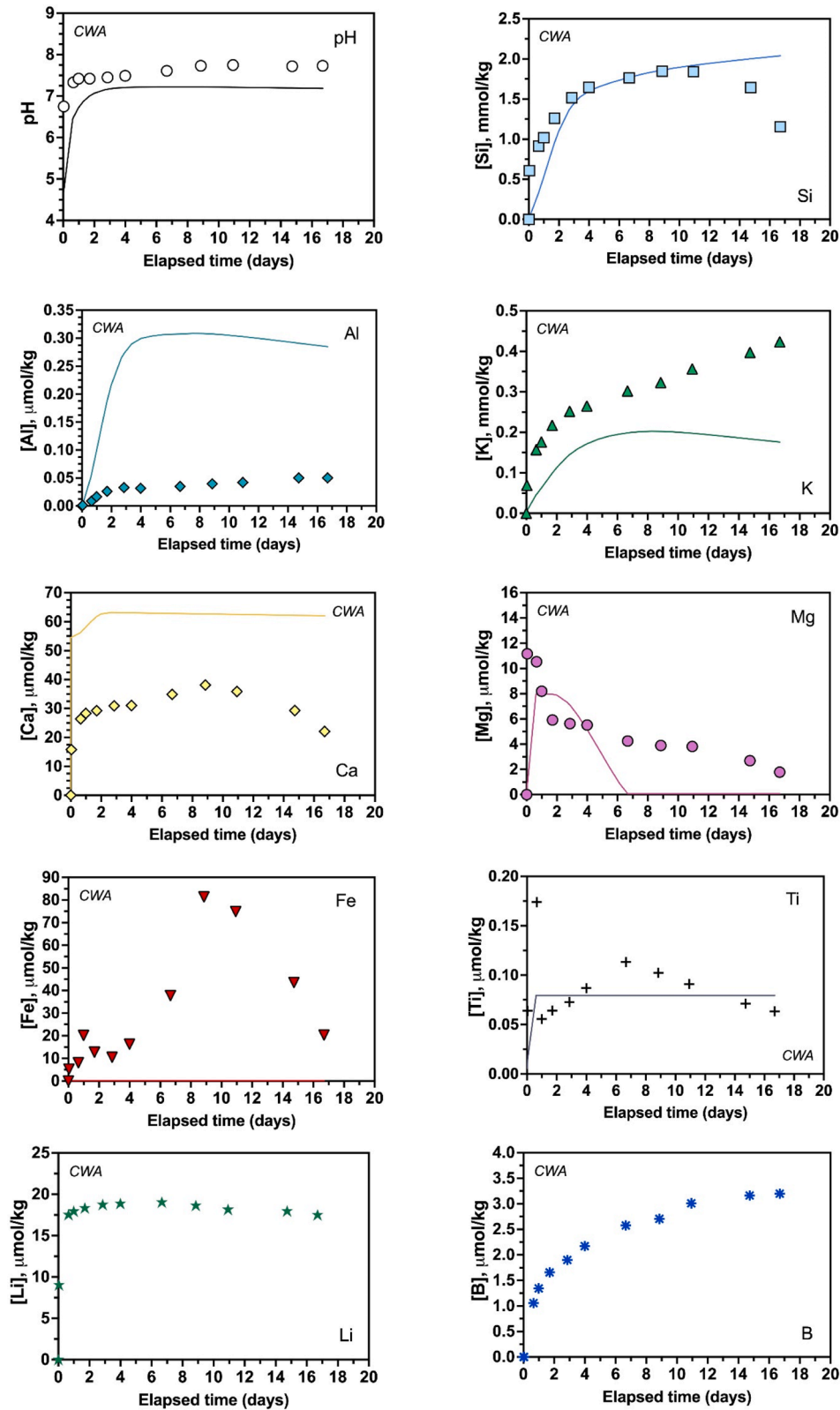
Fig. 5. Comparison between the evolution of reactive fluid concentrations measured during the alteration experiments conducted with static batch Ti-reactor (coloured symbols) and those calculated from the kinetic models (continuous lines). The uncertainties of reported element concentrations are smaller than the size of the symbols. (a) Batch experiment conducted with a starting solution at pH = 4.0 (CWA); (b) batch experiment conducted with an initial solution pH = 10.7 (CWB). The experimental pH values at 180 °C were recalculated from the measurements at 20 °C using the EQ3/6 code (Wolery, 2010).

b. *Experimental data and kinetic model of Expt. CWB*
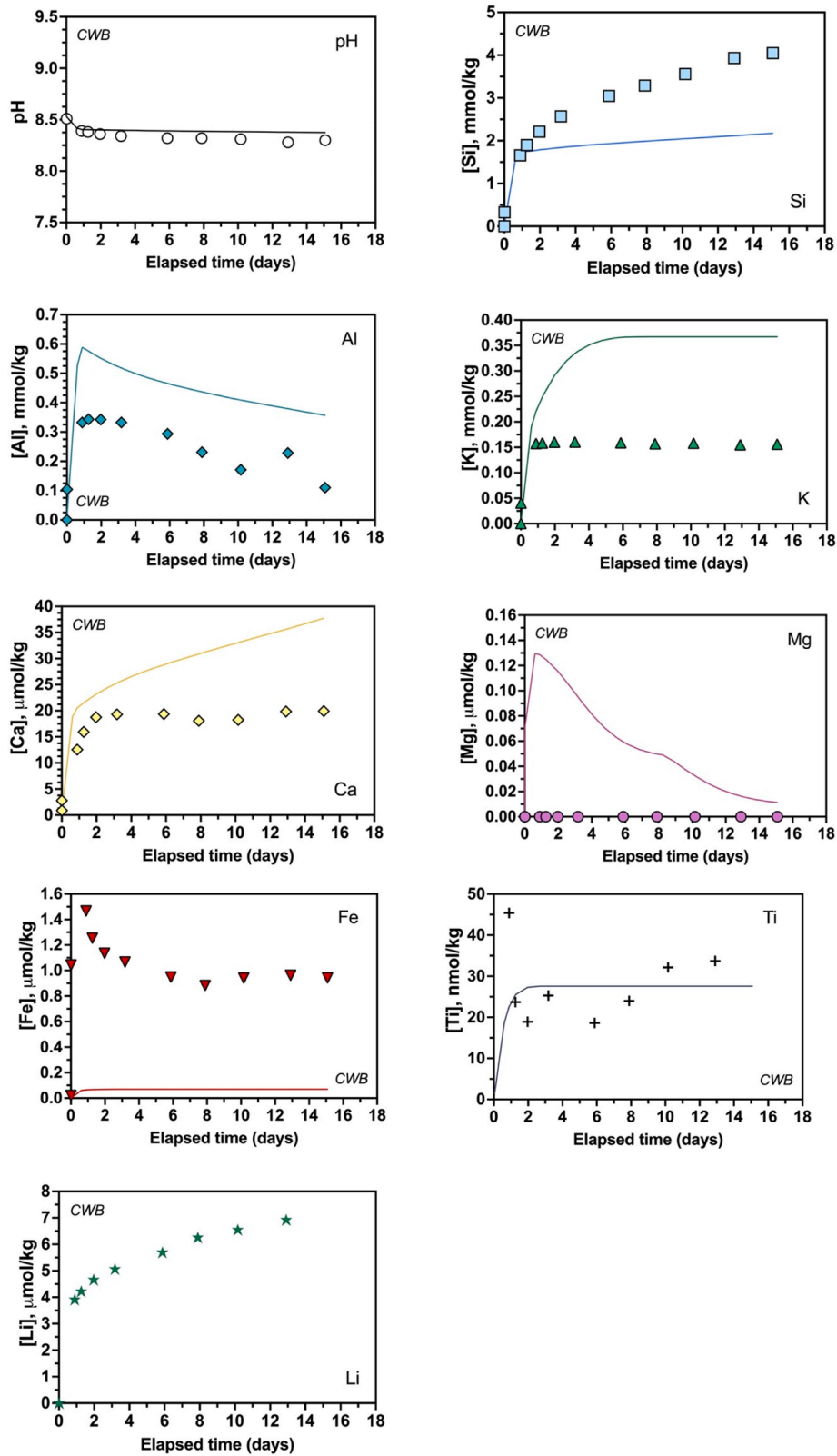
Fig. 5. (*continued*).
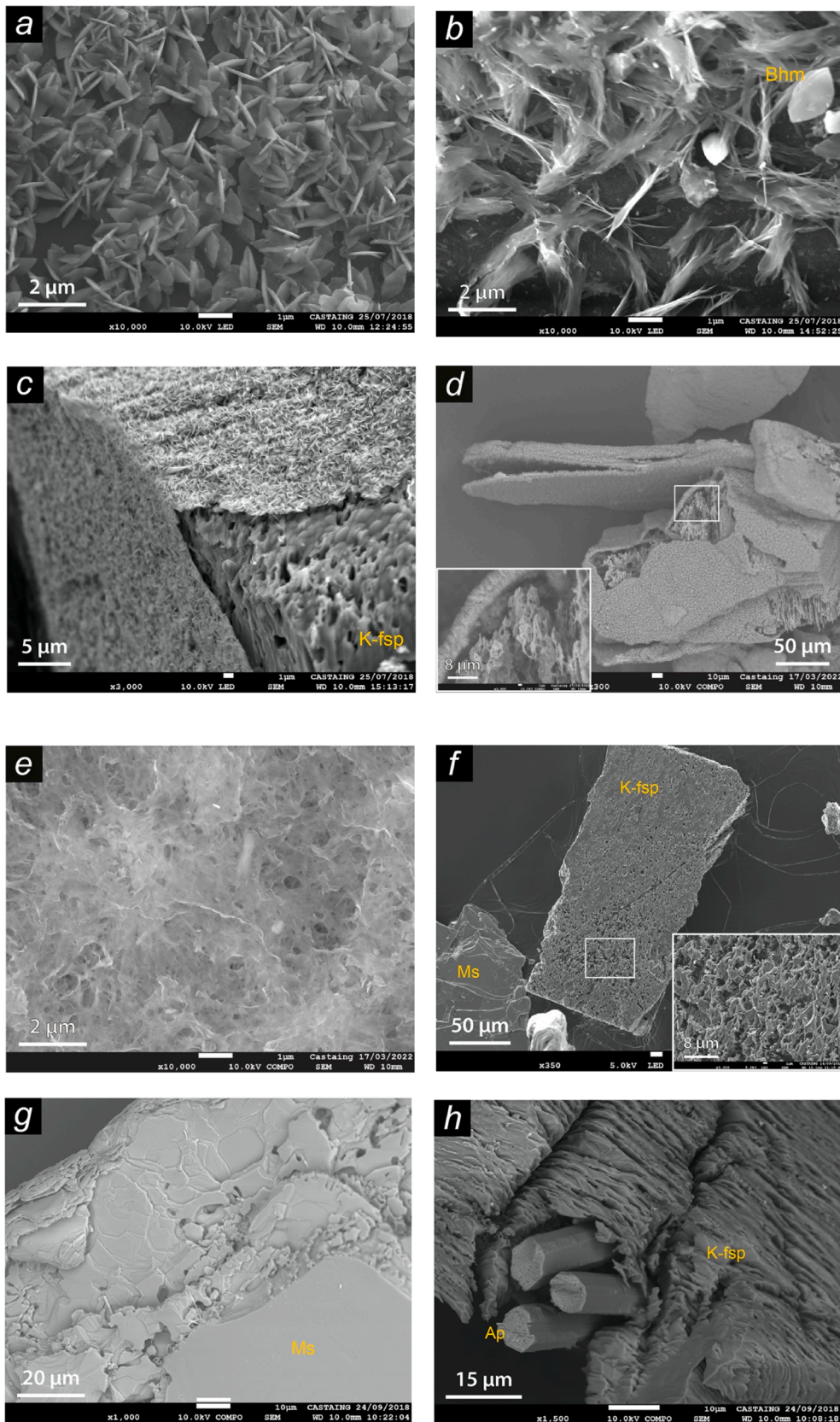
Fig. 6. SEM microphotographs of the granite powder after reaction at 180 °C at different pH in a mixed-flow reactor. (a) Particles of gibbsite and boehmite precipitated on a quartz grain at pH ≈ 4.5 (expt. CW1). (b) Secondary clay minerals (probably illite) formed on quartz surface at pH = 3.1 (expt. CW2). (c) Extensively dissolved K-feldspar crystal embedded in a coating of secondary phases, mainly boehmite and kaolinite (expt. CW2, pH = 3.1). (d) Strongly corroded K-feldspar and mica grains covered by a dense coating of secondary Al-phases (kaolinite, gibbsite, boehmite) at pH = 2.1 (expt. CW7). (e) coating of secondary clay-minerals (chlorite-smectite) found on mica grains at pH = 2.1. (f) deeply pitted crystal of K-feldspar after reaction at pH = 8.0 (expt. CW3): as shown in the inset the surface is very rough and porous as a consequence of the intense leaching. (g) Highly altered muscovite grain after reaction at pH = 8.5 (expt. CW5). (h) Apatite prisms sticking out of a corroded K-feldspar grain (expt. CW5).
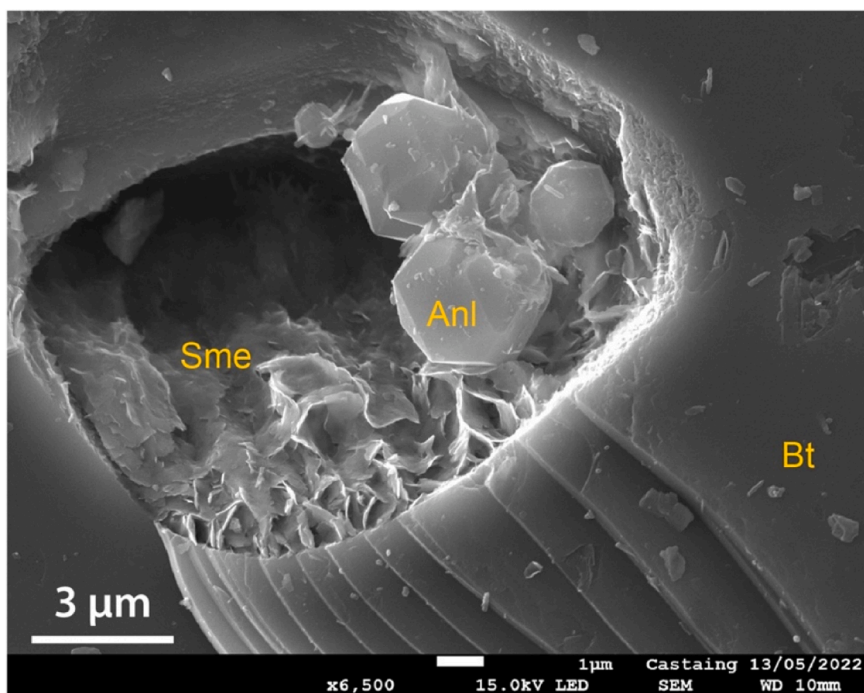
Fig. 7. SEM image of analcime crystals (Anl) and clay minerals (illite/smectite, Sme) formed on a mica grain during the batch experiment CWB, conducted at 180 °C under alkaline conditions (pH = 10.7 at 20 °C).

the geochemical code EQ3/6 (Wolery, 2010).

3.1. Mixed-flow reactor experiments

The plots of Fig. 4 show that a chemical steady state was generally attained during the MFR experiments conducted at different aqueous solution pH, as displayed by the constant concentration levels reached by Si, Al, K and Mg. Different concentration profiles are instead exhibited by Ca. Being a minor constituent of the rock (CaO = 1.0% wt) and likely present in minor but more reactive minerals than plagioclase, such as apatite and possibly calcite, its content in the granite powder was progressively reduced during the experiments, as shown by the decreasing concentrations at acid to mildly acidic pH's (Fig. 4a-b). This pattern is not evident at basic pH, where these Ca-bearing phases dissolve at much slower rates and aqueous Ca concentrations may eventually be controlled by the dissolution of the more abundant plagioclase. Na concentrations are reported only for the experiment at pH 2 (expt. CW7) because all the other experiments were conducted in initial fluids containing 0.01 M of Na. This Na concentration of the fluid phase obscured the contribution coming from the Na-bearing minerals of the rock.

Although the mixed-flow reactor experiments were performed at far from equilibrium conditions with respect to most primary minerals, some secondary phases, mostly Al-rich phases, were observed by SEM analyses of the post-reaction solids. Boehmite (AlOOH), gibbsite (Al(OH)$_3$), kaolinite (Al$_2$Si$_2$O$_5$(OH)$_4$) and other secondary minerals such as chlorite-smectite or illite were identified by EDX analyses and on the basis of their characteristic morphologies. These phases were observed to form at acidic to near neutral pH conditions and occurring mainly as coatings of micrometric crystals on grains of feldspar, quartz and micas (Fig. 6a-e). The granite powder reacted at basic pH conditions (pH 8–8.5 at 180 °C) showed evidence of extensive corrosion with the development of highly porous and rough surface on quartz and feldspars and pervasive exfoliation and pitting of mica grains (Fig. 6f-g). The occurrence of secondary phases forming during the reaction at these conditions, however, was very limited compared to acidic conditions.

3.2. Static batch reactor experiments

The evolution of the fluid composition during the two batch experiments conducted at initially acid (pH = 4.0) and basic conditions (pH = 10.7) shows that the system did not attain a chemical steady state for most of the analysed elements after the two weeks of reaction (Fig. 5). This is particularly evident from the constant increase of K concentration during the experiment CWA and the increasing Si concentration of experiment CWB. These increasing concentrations indicate the continuing dissolution of primary minerals while some secondary phases also formed. The precipitation of secondary solids is suggested by the decrease in Si, Mg, Ca and Fe concentrations with time and the low concentrations of Al relative to the other elements in experiment CWA, whereas the higher Al fluid content and the concentration profiles of the other elements, except for Mg, indicate a minor role of secondary phases formation during experiment CWB. Analyses of the reacted solids by SEM revealed the presence of disseminated boehmite and Fe-oxide crystals along with sparse aggregates of platy/acicular crystals resembling illite/chlorite (not shown) for experiment CWA, whereas the formation of diffuse crystals of analcime (NaAlSi$_2$O$_6$•H$_2$O) and the presence of secondary clay minerals were evident from the analyses of the solid from experiment CWB (Fig. 7).

4. Geochemical modelling results

The results of the comprehensive modelling calculations performed to simulate and interpret the experimental data are reported as continuous curves on the concentration plots of Figs. 4 and 5, where the modelled and measured elemental concentrations are compared. It can be observed that the agreement between the model predictions and the experimental data is generally reasonable, considering the uncertainties and approximations implied by the model (see next section) and the large pH range over which the model was applied. Because the model parameters were initially adjusted to provide a closest fit to the results of experiment CW3, conducted in the MFR at basic conditions, the model does not replicate the experimental observations as well at acid pH, reflecting some of the limitations and unknowns inherent in the model

Table 8

Estimated masses of rock dissolved and corresponding volume change for each of the experiments conducted in this study as calculated by the geochemical model. Masses and volumes are expressed relative to the unit volume (m^3) of the medium (fluid+solid).

Experiment	pH (180 °C)	Rock mass dissolved kg/$m^3_{(medium)}$	Solid mass precipitated kg/$m^3_{(medium)}$	Rock mass change kg/$m^3_{(medium)}$	Volume change dm^3/$m^3_{(medium)}$
CW1	4.6–5.8	0.33	0.056	−0.27	−0.10
CW2	3.1	1.04	0.223	−0.82	−0.32
CW3	8.0	0.83	0.000	−0.83	−0.31
CW5	8.5	1.25	0.000	−1.25	−0.48
CW7	2.1	2.03	0.255	−1.78	−0.69
CWA	6.8–7.7	0.20	0.024	−0.18	−0.06
CWB	8.3–8.5	0.29	0.098	−0.19	−0.06

calculations. In particular, the Si (and Na) concentrations predicted by the model are in poorer agreement with the corresponding measured values at acid pH (expts. CW2 and CW7) than at basic pH (expts. CW3 and CW5). It is evident from the comparison between modelled and experimental data that the same match quality cannot be reached for all the elements nor for the same element at different pH. The model calculations generally overestimate fluid Al concentrations relative to the experimental data, except for CW1, for which the measured concentrations are up to four times higher than those calculated by the model (Fig. 4a); Ca concentrations are well reproduced by the model at pH 2, 7.5 and 8.5 but underestimated at pH 3–7.5 (expts. CW1, CW2, CWA); aqueous Fe concentrations from the model are very close to those measured in the aqueous samples for three of the five MFR experiments, but very low compared to the experimental data in the remaining MFR and SBR experiments. Finally, it has to be noted that the modelled concentration evolution of several elements for the batch experiments starts to diverge from the measured concentration profiles after the first 6–10 days of reaction (K, Si, Ca and Mg for CWA; Si, Ca and Al for CWB).

The kinetic model calculations allow us to estimate the masses and corresponding volumes of primary minerals dissolved and secondary phases precipitated during the experiments. The balance between the two provides insights into the impact of the alteration process on the evolution of rock porosity and permeability as a function of the fluid pH. The calculated amounts of mineral dissolved and precipitated during the course of the experiments are summarized in Table 8 and are illustrated for experiments CW5, CW7 and CWA in Fig. 8. Solid masses and volumes are here referred to the unit volume of the medium, which defines our system (fluid + solid). The experiments CW7 (pH 2) and CW5 (pH 8.5) represent the two pH extremes at which the largest mass of primary minerals dissolved. In both cases plagioclase and K-feldspar alone account for more than 90% of the mass dissolved by the reactions, with a higher amount of K-feldspar dissolved relative to plagioclase at basic conditions. The next phase to be dissolved in higher amounts is quartz (∼ 6% and 2% at pH 2 and 8.5, respectively). Different mineral quantities were instead dissolved during the batch experiments, where quartz amounts to 55% (CWA) and 34% (CWB) of the entire mass dissolved and feldspars account respectively for 35 and 57%.

Secondary phase precipitation is calculated to be most important for the experiments conducted at pH 2 and pH 3 (Fig. 8b and Table 8) where Al-phases (boehmite, gibbsite and kaolinite) are most prominent. In contrast, no secondary phases were calculated to have formed at pH 8 and 8.5 (expts. CW3 & CW5). Lower to negligible masses of secondary phases are predicted to have precipitated during the two batch experiments. In the case of experiment CWA, the model indicates that boehmite is the first phase to form followed by Ca- and K-montmorillonites and illite (Fig. 8e-f), whereas analcime is the main secondary product (0.44 mol/m^3_{medium}) forming during the experiment CWB, with only a minor amount (0.08 mmol/m^3_{medium}) of Ca-montmorillonite (not shown). The formation of illite and Ca-montmorillonite during the two

SBR experiments is also suggested by the activity plots of Fig. 9, which show that the compositions of the respective aqueous samples fall in the stability fields of these two phases. The model could not account for the kinetic formation of analcime because its precipitation rates are poorly known and not easily deducible from existing studies (e.g., Wilkin and Barnes, 2000). The formation of this secondary phase, however, was integrated into the model according to a local equilibrium condition (cf. Wolery and Jarek, 2003; Lucas et al., 2020), which involves analcime instantaneous precipitation when the fluid reaches the saturation condition ($Q/K = 1$).

In all cases the mass balance between dissolved and precipitated minerals indicates that the volume changes are negative (Table 8) but comparatively small for the batch experiments (< 0.1 dm^3/m^3_{medium}), where the total amount of secondary phases predicted to form is likely within the uncertainties of the model.

5. Discussion

The comparison of the geochemical model results with the experimental data show that the model predictions are generally in acceptable agreement with the major element concentrations measured in the fluid samples collected during the experiments. The model fit required some changes to the initially estimated SSA values of microcline, anorthite and chlorite to reach a closer correspondence with the measured concentrations. Although such modifications of SSA were essential to improve the agreement between model calculations and experimental data, the same level of accuracy could not be obtained for all the experiments. The observed discrepancies between experimental data and model results are indicative of the several uncertainties and limitations of the model. The factors that most affected the accuracy of model predictions are briefly discussed below.

5.1. Mineral surface area approximations

The surface area estimates based on grain size and simple geometric assumptions do not always provide a realistic measure of the reactive surface area of mineral grains, as they do not consider the mineral surface roughness and internal porosity, which both contribute to the available mineral-fluid interfacial surface area during chemical reactions. Analogously, it is difficult to estimate single mineral reactive surface areas from BET measurements of rock powders. Notably, identically sized minerals can have significantly different SSA depending not only on their class and morphology but also on their composition, relative degree of alteration and sample preparation protocols (cf. White and Peterson, 1990; Hodson, 1999; Brantley and Mellott, 2000). The difficulty to attribute appropriate SSA values to single mineral phases has led to the use of SSA and mineral dissolution/precipitation rate constants as fitting parameters in multi-scale reactive transport models (e.g., Azaroual and Fouillac, 1997; Soler and Mäder, 2007; Savage et al., 2011; Aradóttir et al., 2015). In our study, it was not possible to reach a good match between modelled and measured concentrations without adjusting the mineral SSA values. An example of model calculations with no adjustment to the estimated SSA is illustrated in Fig. 10 for the experiment CW3. The calculated concentrations of K and Ca plot very far from the measured values compared to the model using modified SSA (Fig. 4c). The increase of the geometric SSA values of anorthite and microcline by factors of 3.5 and 50, respectively, and the parallel decrease of the SSA initially assigned to chlorite by a factor of 40 allowed reaching a much better agreement of the model results with the experimental observations. Even if such corrections may seem arbitrary, they provide some account for the contribution of surface microtopography and internal porosity to the reactivity of feldspars (cf. White, 1995) and for the limited reactivity of many clay minerals, the dissolution of which takes place primarily at edge faces (e.g., Bickmore et al., 2001), which represent only a small fraction of the total surface compared to the nearly inert basal planes (cf. Macht et al., 2011).
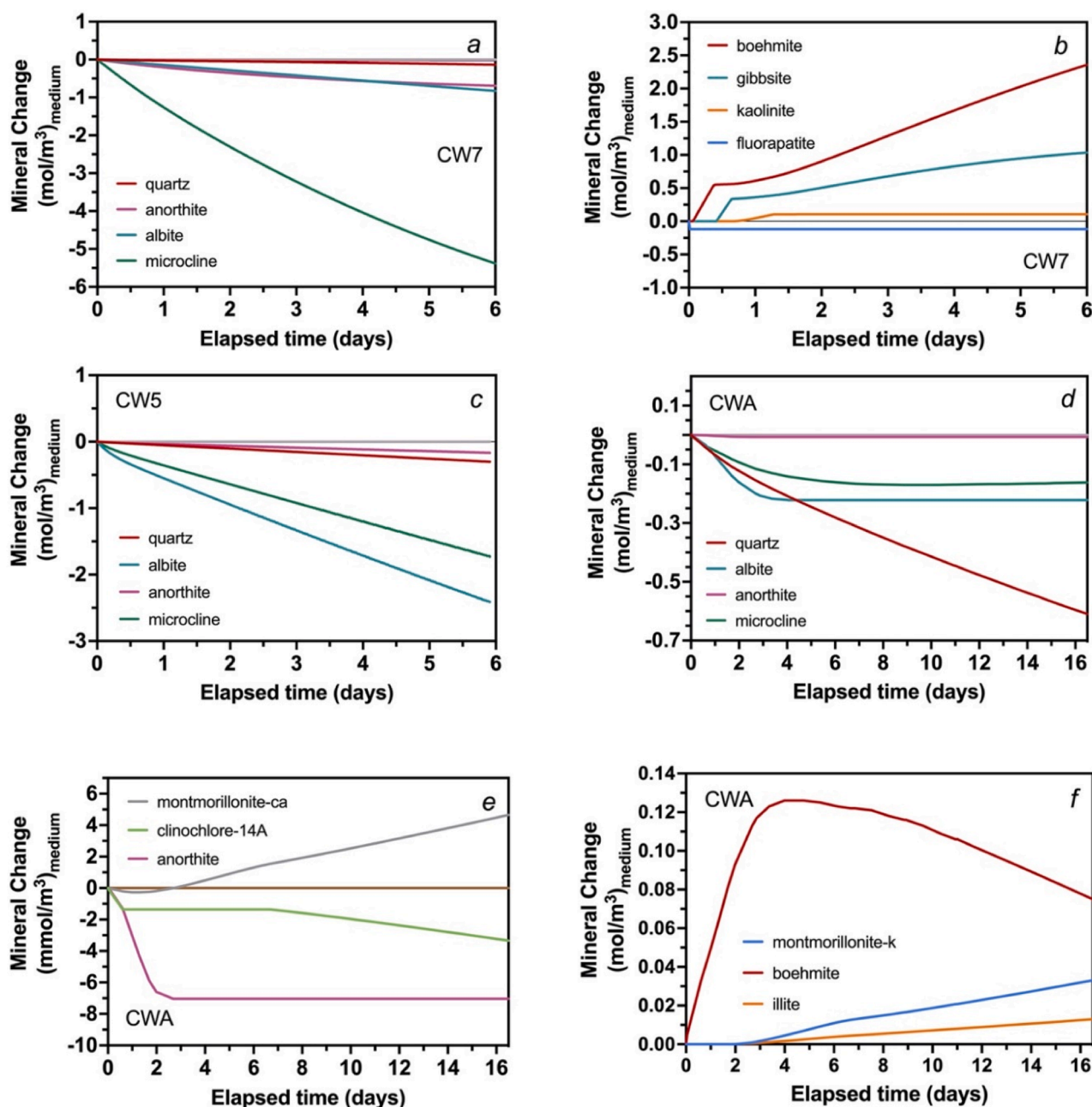
Fig. 8. Computed masses of minerals dissolved and precipitated during the experiments carried out in this study, as estimated by the kinetic model calculations. Plots a-c show the results for the mixed-flow reactor experiments conducted at pH 2 and pH 8.5 (CW7 and CW5, respectively). Plots d-f report the results for the static batch experiment CWA conducted with a starting solution at pH = 4.

However, exceptions to such a behaviour, where basal planes and edge surfaces exhibit comparable reactivity, are reported in the literature (Brandt et al., 2003; Aldushin et al., 2006).

The SSA of the original granite powder, calculated as the sum of the single mineral adjusted SSA values, each multiplied by the corresponding mineral mass fraction (Table 3), is equal to 0.226 m^2/g, which is only a factor of 2 smaller than the SSA measured by the BET method (0.434 m^2/g). This relative concurrence suggests that the estimated SSA values of the single mineral phases can be representative of the "effective" surface area of the granite powder mineral components, providing a good starting point for model calculations.

As shown by the SEM analyses of the post-experiment granite powders (Fig. 5) the rock hydrothermal alteration significantly transforms the morphology and the physical properties of the mineral grains by increasing their roughness, porosity and/or inducing the formation of coatings that could inhibit the dissolution of the underlying mineral surfaces. During the simulation TOUGHREACT recalculates the reactive surface area of each mineral dissolving or precipitating as mineral masses, particle sizes and volume fractions vary with time, assuming a spherical geometry for the mineral grains. Such an approach, common to most geochemical codes, does not adequately take into account the aforementioned changes of mineral surface properties and may lead with time to a significant deviation of model predictions compared to the real evolution of the system. The apparent increasing discrepancy between simulated and measured concentrations of some elements from the two SBR experiments described above (Fig. 5) might reflect the inability of the model to describe the real evolution of mineral surface areas and reactivity over relatively long reaction times.
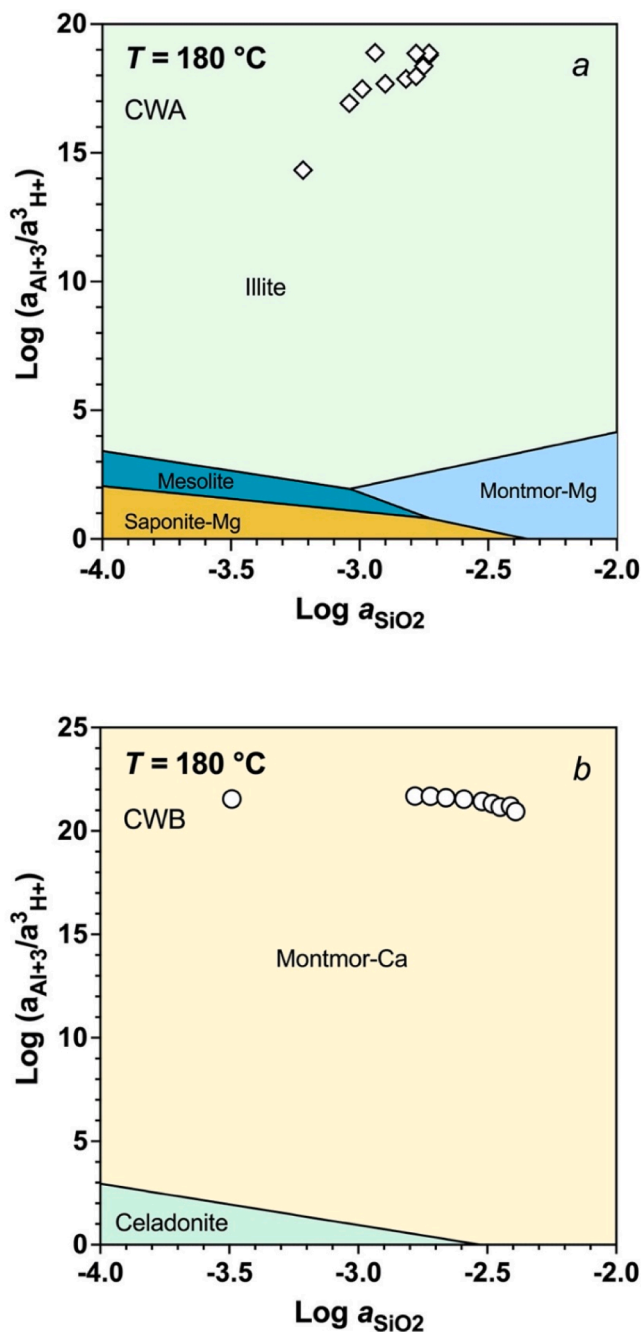
Fig. 9. Activity plots representing the stability fields of relevant granite secondary phases and the calculated aqueous fluid compositions (symbols) of the two static batch experiments, CWA and CWB, conducted respectively at initially acidic pH (a) and basic pH conditions (b). The phase boundary relations were calculated considering the average activity values of the main dissolved ions (K, Mg, Ca) from the two experiments and a constant NaCl concentration of 0.01 M at 180 °C. Several secondary minerals, unlikely to form under the investigated conditions, were excluded from these calculations. The stability limits of the reported mineral phases were calculated using the code GWB (Bethke, 2008).

The study of the morphologic evolution of mineral surfaces and the formation of coatings or secondary phases, which may slow the access of the fluid to the dissolving minerals, is of great importance to quantify the variation of mineral surface reactivity as a function of the reaction progress (cf. Daval et al., 2018; Wild et al., 2019). The intrinsic variability of mineral dissolution rates and their complex dependence on surface structure and morphology (Daval et al., 2013; Godinho et al.,

2014; Pollet-Villard et al., 2016; Lange et al., 2021) suggest that a single model might not be sufficient to describe with acceptable approximation the change of surface area and the corresponding effect on the dissolution rates. The implementation of empirical formulations that describe the temporal evolution of mineral surface parameters and coating development should help, however, to improve the accuracy of reactive transport models and their application to various geochemical processes.

5.2. Rate equations and model accuracy

The agreement between model results and experimental observations depends on the correct estimate of the mineral surface areas and their temporal evolution but is greatly affected by the accuracy of the rate equations used to describe mineral dissolution and precipitation reactions. Particularly critical to our system is the dissolution/precipitation of Al-bearing phases. The comparison between modelled and measured Al concentrations from the MFR experiments suggests that our model calculations either underestimate the formation of secondary Al-phases or overestimate the rates of feldspar dissolution. Note that, by reason of their small amounts in the granite powder and their sluggish reactivity compared to feldspars, the contribution of muscovite and biotite to the Al mass balance can be neglected to a first approximation. With the only exception of experiment CW1, calculated Al concentrations result visibly higher (2–6 times) than the measured values, especially at acidic conditions where secondary Al-phases were found to be more abundant (expts. CW2 and CW7). The interpretation of this difference is not unequivocal, however, as dissolution and precipitation reactions are strongly coupled and an increase of the precipitation rates of Al-phases could accelerate the dissolution of the feldspars (cf. Ganor et al., 2007). In addition, feldspar dissolution rates exhibit a minimum in the near-neutral pH region (cf. Hellmann, 1994; Schott et al., 2009), where a solubility minimum is observed for Al (Bourcier et al., 1993; Wesolowsky and Palmer, 1994; Bénézeth et al., 2001). At such pH conditions the rates of secondary Al-phases formation are controlled by the slower dissolution rates of the primary Al-silicates, consistent with the lower amounts of Al-phases (gibbsite, boehmite) observed at pH 5–6 (expt. CW1) relative to more acidic pH. Nonetheless, the difference between modelled and measured Al, Si and Na concentrations suggests that albite dissolution may be underestimated by the model at acid to near-neutral conditions, which implies that the precipitation of secondary Al-phases is slower in the model calculations than observed experimentally. In contrast, modelled feldspar dissolution rates for experiment CW5, conducted at pH 8.5, appear to be overestimated, as both calculated Al and K concentrations are higher than the corresponding measured values and the presence of observed secondary phases is very limited. It should be kept in mind that the optimization of the model parameters, i.e., the adjustment of some SSA values, was made to provide a best fit to the experimental data acquired at pH 8 (expt. CW3). Therefore, it is not unexpected that the model accuracy changes as one moves away from the conditions for which the model was initially calibrated, especially considering the important role of secondary phases at lower pH, where a bigger discrepancy between model calculations and experimental data are observed.

Although the observed differences between calculated and measured fluid concentrations, in some cases, may not be bigger than the uncertainties implicit in the used rate equations, the accurate characterization of the investigated granite-fluid system call for the improvement of several model parameters, concerning particularly the description of the precipitation reactions and the rate dependence on the distance from thermodynamic equilibrium.

Note that several approximations were introduced in the model to define the rates of mineral precipitation reactions. Precipitation rate equations were assumed to be the same as for dissolution while identical rate constants were attributed to different Al-bearing phases, namely to boehmite and gibbsite and to illite and muscovite (see Table 7).

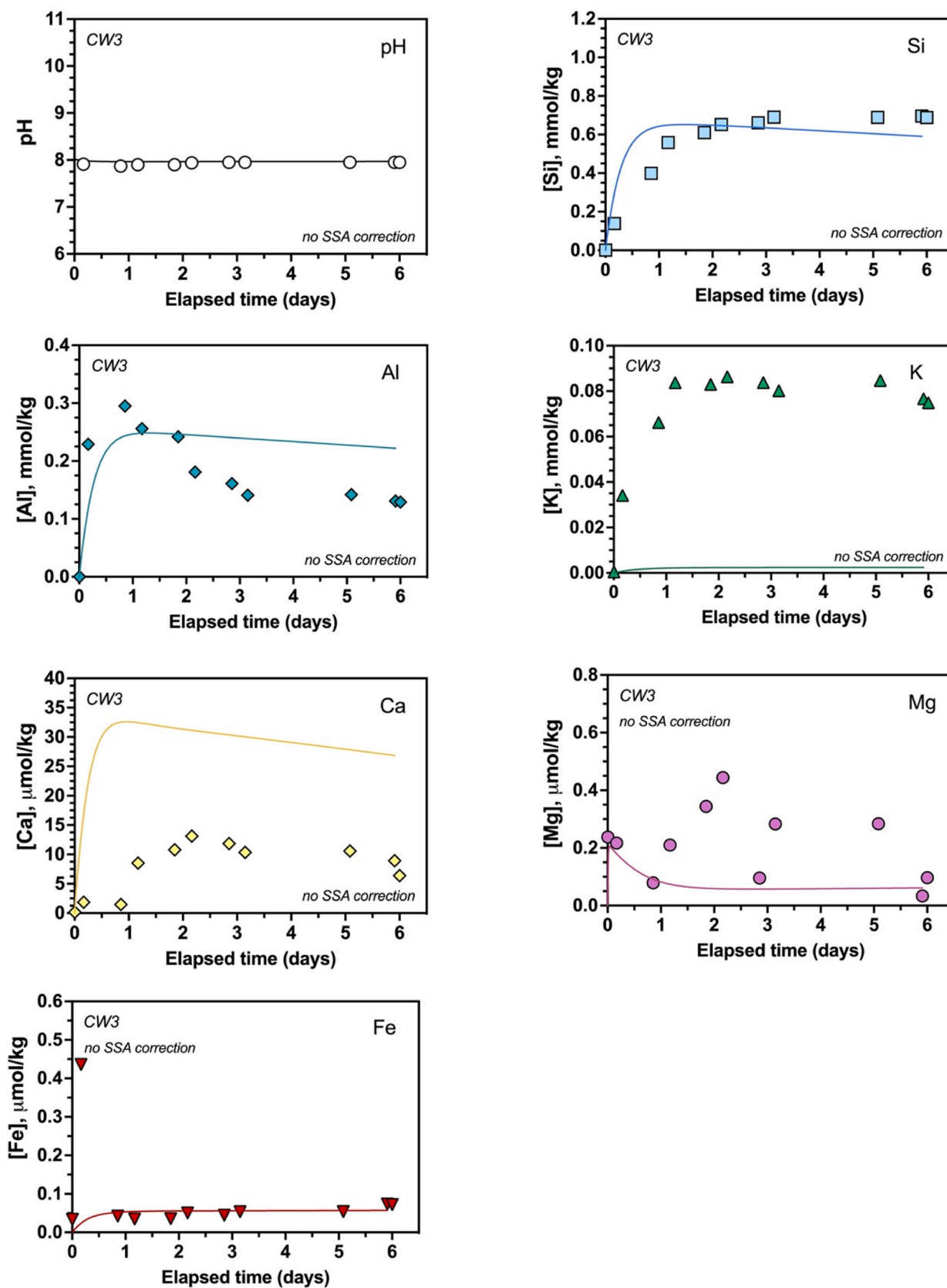**Fig. 10.** Modelled fluid elemental concentrations of experiment CW3 (continuous lines), obtained with no adjustments to the initially estimated mineral SSA, compared with the corresponding measured concentrations (coloured symbols). Note the lower agreement of the model with the measured Ca and K concentrations relative to the model that used modified SSA values for anorthite, K-feldspar and chlorite (Fig. 4c).

Boehmite and gibbsite dissolution and precipitation were determined at 100 and 50 °C, respectively. These rates can be described by the same first order rate equation in proximity of thermodynamic equilibrium at neutral to basic pH (Bénézeth et al., 2008), but there is no evidence that the two phases dissolve/precipitate at nearly the same rate under identical conditions. In addition, gibbsite dissolution and precipitation were reported to show a different dependence on the Gibbs free energy when far from equilibrium (Nagy and Lasaga, 1992), so that the use of the same rate equations and parameters to describe both dissolution and precipitation can be a source of inaccuracies for the model. The same argument applies to the other relevant secondary phases included in our system (illite, kaolinite, and montmorillonite), the precipitation rates of which were defined using the corresponding rate equations of dissolution provided by Palandri and Kharaka (2004). Unfortunately, data on the precipitation rates of relevant secondary phases are sparse in the literature and difficult to extrapolate to the studied conditions via specific rate expressions. Accurate modelling of precipitation reactions would also require introducing the nucleation process into the geochemical model. Several numerical models have been developed to describe the nucleation and growth of minerals and surface precipitates (e.g., Fritz et al., 2009; Noguera et al., 2011; Yang et al., 2022), but their implementation in reactive transport models is not straightforward, as it requires the determination of specific nucleation parameters, including surface energy, nucleation frequency pre-factor, and critical supersaturation, which are, for the most part, unknown.

Several studies showed that the rate dependence of dissolution or precipitation reactions on the Gibbs free energy term $(1 - (Q/K)^m)$ for minerals such as albite, kaolinite and quartz can change as a function of the distance from equilibrium and of the surface reaction history (Gautier, 1999; Hellmann and Tisserand, 2006; Yang and Steefel, 2008; Pollet-Villard et al., 2016). Consequently, the use of the traditional transition-state theory function expressed by Eq. (4) may not be always adequate to describe the rate of these reactions and could introduce additional uncertainties into the model calculations. The studies that demonstrated the suitability of alternative rate equations are, however, limited to few mineral phases and to a narrow range of pH and temperature conditions and don't allow the direct application of such rate equations to our system.

Finally, it should be noted that the effects of other processes such as surface complexation/adsorption and ion exchange are not considered by the model developed in the present study because of the lack of relevant high temperature data. Even if the results of the model are sufficiently close to the experimental data, we cannot exclude the possibility that these processes affect, to some extent, the measured aqueous fluid concentrations (cf. Viani and Bruton, 1996), promoting also the heterogeneous nucleation of secondary phases or the formation of surface altered layers, as reported by previous studies (e.g., Gallup, 1997; Saldi et al., 2015).

6. Summary and conclusions

The hydrothermal alteration of a medium-grained granite from the Carnmenellis pluton was investigated at 180 °C as a function of aqueous solution pH ($2 \leq pH \leq 8.5$) and for experimental durations of 4 to 17 days, using both mixed-flow and static batch reactors. The alteration process was dominated by the dissolution of feldspars and quartz and by the precipitation of boehmite, gibbsite, and kaolinite, with minor amounts of illites, smectites and analcime. Secondary mineral precipitation was more significant at acidic conditions.

The modelling of the experimental data by TOUGHREACT, using mineral rate equations and kinetic parameters taken from Palandri and Kharaka (2004), showed that the code could reproduce reasonably well the experimental data, with differences between modelled and measured elemental fluxes that were within the same order of magnitude. Nevertheless, the model did not match the experimental data with the same accuracy at different pH, showing that its precision decreased outside the conditions for which it was initially optimized. This suggests that the adjustment of some critical model parameters, such as rate constants of dissolution/precipitation, SSA, redox potential, etc., will always be necessary to improve the model performance when moving from a system to another. In addition, the comparison between model results and experimental observations suggests that the model assumptions might not be adequate to simulate longer-term experiments and different interaction scenarios, where the predicted changes of mineral surfaces, the type and amounts of secondary phases, and the inferred impact on parameters such as porosity and permeability (e.g., Lucas et al., 2020) could considerably differ from the real evolution of the system. In particular, the model underestimates the precipitation rates of secondary Al-bearing phases. The formation of such phases can be at the origin of important scaling phenomena in geothermal systems (Newton et al., 2018) and should be better quantified.

The improvement of geochemical model performance over longer timescales requires a better understanding of the processes that modify the structure and reactivity of mineral surfaces with time and control the formation of secondary phases. The quantitative description of mineral-specific changes of surface roughness and secondary porosity, the formation of amorphous silica surface coatings, and the nucleation and growth of clay minerals and secondary Al-bearing phases are key for the further development of reactive transport models and their application to geothermal systems. In addition, determining the type of secondary phases and their precipitation rates is critical not only to estimate the local distribution and change of permeability, but also to assess the reactivity of fracture surfaces, their mechanical behaviour and the induced changes to the fluid flow (Davatzes and Hickman, 2010; Dobson et al., 2021). It is anticipated that the improved description of these processes will increase the predictive abilities of thermal-hydrological-mechanical-chemical models and help the development of more effective technologies to extend the lifetime of EGS and minimize their environmental impact.

Table A.1–1
Fluid chemical data of experiment **CW1**. conducted at 180 °C and initial fluid pH = 3.99: Chemical data obtained from ICP-OES analyses.

Sample ID	time (days)	pH (20 °C)	pH (180 °C)	Al M	Si M	K M	Ca M	Mg M
CW1–1	0.0	4.45	4.38	3.5E-07	1.02E-04	3.26E-05	6.54E-06	4.54E-06
CW1–2	0.7	6.89	6.60	3.96E-06	4.21E-04	7.37E-05	2.98E-05	2.58E-06
CW1–3	0.9	6.89	6.33	6.17E-06	4.20E-04	6.75E-05	2.87E-05	2.55E-06
CW1–4	1.0	–	6.48	5.07E-06	4.24E-04	6.96E-05	2.89E-05	2.59E-06
CW1–5	1.7	6.72	5.09	9.12E-06	4.26E-04	6.64E-05	1.91E-05	2.31E-06
CW1–6	2.0	6.65	4.95	8.01E-06	4.27E-04	6.51E-05	1.73E-05	2.37E-06
CW1–7	2.9	–	6.56	1.19E-05	4.22E-04	1.12E-04	1.38E-05	2.20E-06
CW1–8	4.8	6.7	4.50	1.28E-05	4.17E-04	5.76E-05	9.07E-06	1.82E-06
CW1–9	5.0	6.61	4.55	1.22E-05	4.13E-04	5.98E-05	1.02E-05	1.66E-06
CW1–10	5.7	6.61	4.50	1.29E-05	4.18E-04	5.95E-05	8.33E-06	1.65E-06

Table A.1–2

Fluid chemical data of experiment **CW1**. conducted at 180 °C and initial fluid pH = 3.99: Chemical data obtained from ICP-MS analyses. DL = detection limit.

Sample ID	Li μM	Ti μM	Cr μM	Mn μM	Fe μM	Ni μM	Rb μM	Sr μM	Ba μM	B μM
CW1–1	6.38	0.01	4.15	0.36	5.76	0.83	0.33	0.01	< DL	4.53
CW1–2	5.23	0.02	0.11	< DL	0.15	< DL	0.24	0.06	0.01	2.79
CW1–3	4.10	0.02	0.12	< DL	0.09	< DL	0.24	0.07	0.01	2.46
CW1–4	3.34	0.02	0.14	< DL	0.10	< DL	0.24	1.01	0.01	2.76
CW1–5	1.36	0.02	0.23	< DL	0.08	< DL	0.25	0.09	0.02	1.82
CW1–6	1.04	0.02	0.25	< DL	0.08	< DL	0.25	0.09	0.02	1.59
CW1–7	0.50	0.02	0.31	< DL	0.06	< DL	0.25	0.10	0.03	1.14
CW1–8	0.28	0.02	0.21	< DL	0.06	< DL	0.24	0.11	0.04	0.65
CW1–9	0.27	0.02	0.20	< DL	0.06	< DL	0.24	0.12	0.04	0.66
CW1–10	0.26	0.02	0.24	< DL	0.06	< DL	0.24	0.12	0.05	0.48

Table A.2–1

Fluid chemical data of experiment **CW2**. conducted at 180 °C and initial fluid pH = 2.98: Chemical data obtained from ICP-OES analyses.

Sample ID	time (days)	pH (20 °C)	pH (180 °C)	Al M	Si M	K M	Ca M	Mg M
CW2–1	0.0	4.08	3.05	2.23E-06	1.15E-04	4.73E-05	2.58E-05	6.65E-06
CW2–2	0.8	3.37	3.15	3.05E-06	9.94E-04	1.65E-04	6.97E-05	1.02E-05
CW2–3	2.1	3.32	3.13	3.59E-07	1.29E-03	1.86E-04	5.04E-05	4.82E-06
CW2–4	2.7	3.28	3.13	3.30E-07	1.31E-03	1.86E-04	4.60E-05	4.89E-06
CW2–5	2.9	3.3	3.13	2.61E-07	1.28E-03	1.95E-04	4.36E-05	4.68E-06
CW2–6	3.1	3.29	3.13	3.66E-07	1.29E-03	1.96E-04	4.33E-05	4.76E-06
CW2–7	3.7	3.28	3.13	3.13E-07	1.29E-03	1.98E-04	4.15E-05	5.38E-06
CW2–8	3.9	3.29	3.12	2.33E-07	1.27E-03	1.85E-04	3.96E-05	5.22E-06
CW2–9	4.0	3.29	3.13	2.95E-07	1.30E-03	2.04E-04	3.85E-05	5.29E-06

Table A.2–2

Fluid chemical data of experiment **CW2**. conducted at 180 °C and initial fluid pH = 2.98: Chemical data obtained from ICP-MS analyses. DL = detection limit.

Sample ID	Li μM	Ti μM	Cr μM	Mn μM	Fe μM	Ni μM	Rb μM	Sr μM	Ba μM	B μM
CW2–1	7.16	0.01	0.04	0.77	0.30	0.89	0.48	0.22	0.21	0.57
CW2–2	5.74	0.05	0.01	1.22	0.64	0.08	0.56	0.36	0.19	0.69
CW2–3	1.57	0.05	0.01	0.45	0.81	0.07	0.59	0.46	0.36	0.25
CW2–4	1.35	0.05	0.01	0.38	0.91	0.06	0.61	0.45	0.39	0.15
CW2–5	1.30	0.05	0.01	0.36	0.85	0.06	0.61	0.43	0.39	0.17
CW2–6	1.29	0.05	0.01	0.35	0.85	0.06	0.60	0.42	0.39	0.13
CW2–7	1.27	0.05	< DL	0.33	0.93	0.05	0.62	0.39	0.40	0.08
CW2–8	1.25	0.04	0.01	0.33	0.90	0.05	0.62	0.39	0.40	0.07
CW2–9	1.25	0.05	0.01	0.33	0.86	0.05	0.61	0.38	0.40	0.09

CRediT authorship contribution statement

Giuseppe D. Saldi: Conceptualization, Methodology, Investigation, Formal analysis, Data curation, Validation, Writing – original draft, Visualization. **Kevin G. Knauss:** Methodology, Software, Formal analysis, Validation, Data curation, Writing – review & editing. **Nicolas Spycher:** Software, Validation, Data curation, Resources, Writing – review & editing. **Eric H. Oelkers:** Supervision, Resources, Funding acquisition, Writing – review & editing. **Adrian P. Jones:** Project administration, Funding acquisition.

Declaration of Competing Interest

The authors declare that they have no known competing financial interests or personal relationships that could have appeared to influence the work reported in this paper.

Table A.3–1

Fluid chemical data of experiment **CW3**. conducted at 180 °C and initial fluid pH = 9.02: Chemical data obtained from ICP-OES analyses.

Sample ID	time (days)	pH (20 °C)	pH (180 °C)	Al M	Si M	K M	Ca M	Mg M
CW3–1	0.2	8.73	7.91	2.29E-04	1.39E-04	3.41E-05	1.86E-06	2.17E-07
CW3–2	0.9	8.73	7.87	2.95E-04	3.99E-04	6.62E-05	1.46E-06	7.9E-08
CW3–3	1.2	8.84	7.9	2.56E-04	5.59E-04	8.37E-05	8.51E-06	2.10E-07
CW3–4	1.8	8.84	7.9	2.42E-04	6.10E-04	8.30E-05	1.08E-05	3.44E-07
CW3–5	2.2	8.91	7.94	1.81E-04	6.52E-04	8.63E-05	1.31E-05	4.44E-07
CW3–6	2.9	8.9	7.95	1.61E-04	6.61E-04	8.38E-05	1.18E-05	9.6E-08
CW3–7	3.1	8.93	7.95	1.41E-04	6.90E-04	8.02E-05	1.03E-05	2.83E-07
CW3–8	5.1	8.92	7.95	1.42E-04	6.89E-04	8.47E-05	1.06E-05	2.84E-07
CW3–9	5.9	8.93	7.95	1.31E-04	7.67E-05	7.67E-05	8.92E-06	3.3E-08
CW3–10	6.0	8.92	7.95	1.29E-04	6.88E-04	7.49E-05	6.38E-06	9.7E-08

Table A.3–2
Fluid chemical data of experiment **CW3**. conducted at 180 °C and initial fluid pH = 9.02: Chemical data obtained from ICP-MS analyses. DL = detection limit.

Sample ID	Li μM	Ti μM	Cr μM	Mn μM	Fe μM	Ni μM	Rb μM	Sr μM	Ba μM
CW3–1	2.41	0.02	0.34	< DL	0.57	< DL	0.14	0.002	< DL
CW3–2	3.57	< DL	0.85	< DL	0.01	< DL	0.21	< DL	< DL
CW3–3	1.49	0.02	1.21	< DL	0.01	< DL	0.24	0.01	< DL
CW3–4	1.02	0.02	1.09	< DL	0.01	< DL	0.25	0.01	< DL
CW3–5	0.58	0.02	0.88	< DL	0.03	< DL	0.25	0.03	< DL
CW3–6	0.47	0.02	0.85	< DL	0.03	< DL	0.26	0.03	< DL
CW3–7	0.35	0.02	0.78	< DL	0.03	< DL	0.25	0.04	0.003
CW3–8	0.33	0.02	0.77	< DL	0.02	< DL	0.25	0.05	0.004
CW3–9	0.22	0.02	0.74	< DL	0.03	< DL	0.24	0.06	0.008
CW3–10	0.21	0.02	0.73	< DL	0.04	< DL	0.23	0.07	0.011

Table A.4–1
Fluid chemical data of experiment **CW5**. conducted at 180 °C and initial fluid pH = 10.55: Chemical data obtained from ICP-OES analyses. DL = detection limit.

Sample ID	time (days)	pH (20 °C)	pH (180 °C)	Al M	Si M	K M	Ca M	Mg M
CW5–1	0.0	10.13	8.51	9.08E-05	2.89E-04	4.20E-05	2.66E-06	8.20E-07
CW5–2	0.9	9.93	8.46	1.72E-04	1.04E-03	1.02E-04	5.04E-06	7.5E-08
CW5–3	1.6	9.95	8.46	1.49E-04	1.08E-03	9.27E-05	1.06E-05	3.61E-07
CW5–4	1.9	9.93	8.46	1.43E-04	1.08E-03	8.85E-05	1.05E-05	5.2E-08
CW5–5	2.6	9.98	8.46	1.37E-04	1.09E-03	9.11E-05	9.89E-06	1.4E-08
CW5–6	2.9	9.87	8.46	1.40E-04	1.09E-03	8.39E-05	1.24E-05	4.30E-07
CW5–7	3.6	9.95	8.46	1.39E-04	1.07E-03	8.22E-05	9.34E-06	1.89E-07
CW5–8	4.0	9.95	8.46	1.47E-04	1.09E-03	9.34E-05	9.75E-06	< DL
CW5–9	4.6	9.97	8.46	1.44E-04	1.07E-03	8.94E-05	1.08E-05	6.6E-08
CW5–10	5.0	9.94	8.46	1.44E-04	1.06E-03	8.96E-05	9.81E-06	< DL
CW5–11	5.6	9.99	8.46	1.44E-04	1.05E-03	8.40E-05	1.02E-05	< DL

Table A.4–2
Fluid chemical data of experiment **CW5**. conducted at 180 °C and initial fluid pH = 10.55: Chemical data obtained from ICP-MS analyses. DL = detection limit.

Sample ID	Li μM	Ti μM	Cr μM	Mn μM	Fe μM	Ni μM	Rb μM	Sr μM	Ba μM
CW5–1	1.55	0.05	0.29	< DL	0.47	< DL	0.15	< DL	< DL
CW5–2	1.49	0.03	0.67	< DL	0.08	< DL	0.32	0.01	< DL
CW5–3	0.85	0.03	0.49	< DL	0.23	< DL	0.30	0.03	< DL
CW5–4	0.71	0.03	0.46	< DL	0.27	< DL	0.29	0.03	< DL
CW5–5	0.55	0.03	0.42	< DL	0.34	< DL	0.28	0.04	< DL
CW5–6	0.51	0.03	0.42	< DL	0.37	< DL	0.28	0.05	0.005
CW5–7	0.44	0.03	0.43	< DL	0.37	< DL	0.27	0.06	0.007
CW5–8	0.42	0.03	0.44	< DL	0.36	< DL	0.27	0.06	0.008
CW5–9	0.39	0.03	0.44	< DL	0.35	< DL	0.25	0.06	0.009
CW5–10	0.38	0.03	0.45	< DL	0.35	< DL	0.25	0.06	0.010
CW5–11	0.37	0.03	0.46	< DL	0.37	< DL	0.25	0.07	0.013

Table A.5–1
Fluid chemical data of experiment **CW7**. conducted at 180 °C and initial fluid pH = 2.02: Chemical data obtained from ICP-OES analyses.

Sample ID	time (days)	pH (20 °C)	pH (180 °C)	Al M	Fe M	Si M	K M	Ca M	Mg M	Na M
CW7–1	0.0	2.12	2.13	8.47E-05	2.99E-04	4.69E-04	1.32E-04	1.41E-04	4.37E-05	9.70E-05
CW7–2	0.3	2.13	2.16	1.54E-04	1.67E-04	2.42E-03	3.24E-04	1.62E-04	4.49E-05	6.33E-04
CW7–3	0.9	2.10	2.15	7.57E-05	4.49E-05	3.43E-03	3.58E-04	1.44E-04	2.00E-05	9.05E-04
CW7–4	1.2	2.09	2.15	6.79E-05	3.55E-05	3.43E-03	3.69E-04	1.37E-04	1.44E-05	8.79E-04
CW7–5	1.9	2.07	2.14	5.98E-05	2.44E-05	3.18E-03	3.96E-04	1.25E-04	6.00E-06	7.64E-04
CW7–6	3.9	2.04	2.12	4.14E-05	1.48E-05	2.56E-03	4.61E-04	7.84E-05	7.51E-07	4.76E-04
CW7–7	4.2	2.04	2.11	3.92E-05	1.48E-05	2.50E-03	4.66E-04	7.04E-05	7.60E-07	4.41E-04
CW7–8	4.9	2.06	2.11	3.51E-05	1.61E-05	2.29E-03	4.65E-04	5.97E-05	1.83E-06	3.69E-04
CW7–9	5.2	2.06	2.11	3.36E-05	1.76E-05	2.22E-03	4.60E-04	5.25E-05	2.85E-06	4.15E-04
CW7–10	5.9	2.10	2.12	3.18E-05	2.10E-05	2.03E-03	4.50E-04	4.23E-05	5.13E-06	5.14E-04
CW7–11	6.2	2.07	2.10	3.04E-05	2.20E-05	1.96E-03	4.36E-04	3.73E-05	7.07E-06	2.61E-04

Table B.1–1
Fluid chemical data of experiment **CWA**. conducted at 180 °C and initial fluid pH = 4.03: Chemical data obtained from ICP-OES analyses. DL = detection limit.

Sample ID	time (hours)	pH (20 °C)	pH (180 °C)	Volume ml	Al M	Fe M	Si M	K M	Ca M	Mg M
CWA-0	0.0	4.03	–	401.9	< DL	< DL	< DL	< DL	< DL	< DL
CWA-1	0.9	4.26	6.75	389.9	1.21E-06	5.24E-06	5.24E-06	6.07E-04	6.93E-05	1.58E-05
CWA-2	15.7	4.58	7.33	376.6	8.76E-06	8.09E-06	8.09E-06	9.14E-04	1.57E-04	2.64E-05
CWA-3	23.7	5.01	7.42	365.5	1.66E-05	2.01E-05	2.01E-05	1.02E-03	1.76E-04	2.83E-05
CWA-4	40.8	6.1	7.42	353.6	2.63E-05	1.28E-05	1.28E-05	1.26E-03	2.17E-04	2.93E-05
CWA-5	68.6	6.23	7.45	341.8	3.28E-05	1.05E-05	1.05E-05	1.52E-03	2.52E-04	3.09E-05
CWA-6	95.8	6.08	7.49	330.5	3.16E-05	1.63E-05	1.63E-05	1.65E-03	2.65E-04	3.10E-05
CWA-7	160.0	6.44	7.61	319.8	3.49E-05	3.78E-05	3.78E-05	1.76E-03	3.02E-04	3.49E-05
CWA-8	212.5	6.47	7.73	308.4	3.98E-05	8.13E-05	8.13E-05	1.85E-03	3.23E-04	3.81E-05
CWA-9	262.3	6.32	7.75	297.7	4.19E-05	7.49E-05	7.49E-05	1.84E-03	3.57E-04	3.59E-05
CWA-10	353.6	6.55	7.72	285.5	5.01E-05	4.35E-05	4.35E-05	1.64E-03	3.97E-04	2.93E-05
CWA-11	400.7	6.51	7.73	271.4	5.02E-05	2.03E-05	2.03E-05	1.15E-03	4.24E-04	2.20E-05

Table B.1–2
Fluid chemical data of experiment **CWA**. conducted at 180 °C and initial fluid pH = 4.03: Chemical data obtained from ICP-MS analyses. DL = detection limit.

Sample ID	Li μM	Ti μM	Cr μM	Mn μM	Ni μM	Rb μM	Sr μM	Ba μM	B μM
CWA-0	< DL	< DL	< DL	< DL	< DL	< DL	< DL	< DL	< DL
CWA-1	9.03	0.06	0.67	0.19	4.39	0.61	0.03	0.01	< DL
CWA-2	17.53	0.17	0.07	0.16	2.74	0.38	0.02	0.01	1.05
CWA-3	17.94	0.06	0.05	0.29	3.78	0.44	0.03	0.01	1.34
CWA-4	18.33	0.06	0.10	0.21	2.27	0.55	0.03	0.004	1.66
CWA-5	18.74	0.07	0.03	0.16	1.77	0.66	0.03	0.01	1.90
CWA-6	18.88	0.09	0.05	0.26	2.73	0.71	0.03	0.01	2.17
CWA-7	19.04	0.11	0.08	0.61	5.87	0.82	0.04	0.01	2.57
CWA-8	18.65	0.10	0.03	0.94	9.30	0.87	0.06	0.01	2.70
CWA-9	18.15	0.09	0.02	0.78	8.63	0.92	0.06	0.01	3.01
CWA-10	17.96	0.07	0.01	0.48	4.99	1.04	0.06	0.01	3.16
CWA-11	17.51	0.06	0.02	0.25	2.19	1.15	0.06	0.01	3.20

Table B.2–1
Fluid chemical data of experiment **CWB**. conducted at 180 °C and initial fluid pH = 10.66: Chemical data obtained from ICP-OES analyses. DL = detection limit.

Sample ID	time (hours)	pH (20 °C)	pH (180 °C)	Volume ml	Al M	Fe M	Si M	K M	Ca M	Mg M
CWB-0	0.0	10.66	–	265.7	< DL	< DL	< DL	< DL	< DL	< DL
CWB-1	0.3	9.99	8.51	251.2	1.04E-04	1.04E-06	3.27E-04	4.05E-05	8.74E-07	< DL
CWB-2	21.4	9.79	8.39	238.4	3.33E-04	1.47E-06	1.66E-03	1.57E-04	1.25E-05	< DL
CWB-3	30.3	9.72	8.38	226.0	3.44E-04	1.25E-06	1.90E-03	1.59E-04	1.59E-05	< DL
CWB-4	47.2	9.82	8.36	213.1	3.43E-04	1.14E-06	2.21E-03	1.60E-04	1.88E-05	< DL
CWB-5	76.4	9.68	8.34	201.8	3.33E-04	1.07E-06	2.57E-03	1.60E-04	1.93E-05	< DL
CWB-6	141.2	9.39	8.32	189.9	2.93E-04	9.48E-07	3.05E-03	1.59E-04	1.94E-05	< DL
CWB-7	189.3	9.44	8.32	178.0	2.31E-04	8.82E-07	3.29E-03	1.57E-04	1.81E-05	< DL
CWB-8	243.8	9.45	8.31	167.2	1.71E-04	9.41E-07	3.56E-03	1.58E-04	1.82E-05	< DL
CWB-9	309.8	9.43	8.28	156.6	2.28E-04	9.63E-07	3.93E-03	1.55E-04	1.99E-05	< DL
CWB-10	361.8	9.43	8.30	144.0	1.10E-04	9.43E-07	4.05E-03	1.56E-04	1.99E-05	< DL

Table B.2–2
Fluid chemical data of experiment **CWB**. conducted at 180 °C and initial fluid pH = 10.66: Chemical data obtained from ICP-MS analyses. n.a. = not analysed.

Sample ID	Li μM	Ti μM	Cr μM	Mn μM	Ni μM	Rb μM	Sr μM	Mo μM	Cu μM	Zn μM
CWB-0	n.a.	n.a.	n.a.	n.a.	n.a.	n.a.	n.a.	n.a.	n.a.	n.a.
CWB-1	n.a	n.a.	n.a.	n.a.	n.a.	n.a.	n.a.	n.a.	n.a.	n.a.
CWB-2	3.91	0.05	0.52	0.04	0.15	0.41	0.02	0.28	0.10	0.05
CWB-3	4.22	0.02	0.45	0.03	0.09	0.42	0.03	0.30	0.09	0.05
CWB-4	4.66	0.02	0.39	0.02	0.06	0.42	0.03	0.33	0.09	0.06
CWB-5	5.06	0.03	0.39	0.02	0.10	0.42	0.02	0.35	0.10	0.06
CWB-6	5.70	0.02	0.39	0.02	0.15	0.42	0.02	0.38	0.09	0.05
CWB-7	6.26	0.02	0.40	0.02	0.08	0.43	0.01	0.40	0.09	0.05
CWB-8	6.55	0.03	0.39	0.02	0.11	0.41	0.01	0.40	0.09	0.04
CWB-9	6.92	0.03	0.36	0.03	0.12	0.41	0.01	0.41	0.08	0.04
CWB-10	n.a	n.a.	n.a.	n.a.	n.a.	n.a.	n.a.	n.a.	n.a.	n.a.

Data availability

All data are included within the article and available in the Supplementary Materials

Supplementary materials

Supplementary material associated with this article can be found, in the online version, at doi:10.1016/j.geothermics.2022.102633.

Appendix

Summary of all the fluid chemical data from the experiments.

Appendix A

Chemical composition of the fluid samples collected during the granite alteration experiments conducted with the mixed-flow reactor.

Appendix B

Chemical composition of the fluid samples collected during the granite alteration experiments conducted with the static batch reactor.

References

Afifi, A.A., Bricker, O.P., Chemerys, J.C., 1985. Experimental chemical weathering of various bedrock types at different pH-values 1. Sandstone and granite. Chem. Geol. 49, 87–113.

Aldushin, K., Jordan, G., Schmahl, W.W., 2006. Basal plane reactivity of phyllosilicates studied in situ by hydrothermal atomic force microscopy (HAFM). Geochim. Cosmochim. Acta 70, 4380–4391.

André, L., Rabemanana, V., Vuataz, F.-D, 2006. Influence of water–rock interactions on fracture permeability of the deep reservoir at Soultz-sous-Forêts, France. Geothermics 35, 507–531.

Appelo, C.A.J., 1994. Some calculations on multicomponent transport with cation exchange in aquifers. Ground Water 32, 968–975.

Aqui, A.R., Zarrouk, S., 2011. Permeability enhancement of conventional geothermal wells. In: Proceedings New Zealand Geothermal Workshop 2011.

Aquilina, L., Pauwels, H., Gwenter, A., Fouillac, C., 1997. Water-rock interaction processes in the Triassic sandstone and the granitic basement of the Rhine Graben: geochemical investigation of a geothermal reservoir. Geochim. Cosmochim. Acta 61, 4281–4295.

Aradóttir, E.S.P., Gunnarsson, I., Sigfússon, B., Gunnarsson, G., Júliusson, B.M., et al., 2015. Toward cleaner geothermal energy utilization: capturing and sequestering CO₂ and H₂S emissions from geothermal power plants. Transp. Porous Med. 108, 61–84.

Azaroual, M., Fouillac, C., 1997. Experimental study and modelling of granite-distilled water interactions at 180 °C and 14 bars. Geochim. Cosmochim. Acta 12, 55–73.

Bächler, D., Kohl, T., 2005. Coupled thermal–hydraulic–chemical modelling of enhanced geothermal systems. Geophys. J. Int. 161, 533–548.

Bandstra, J.Z., Buss, H.L., Campen, R.K., Liermann, L.J., Moore, J., Hausrath, E.M., Navarre-Sitchler, A.K., Jang, J.H., Brantley, S.L., 2008. Appendix: compilation of mineral dissolution rates. In: Brantley, S.L., Kubicki, J.D., White, A.F. (Eds.), Kinetics of Water–Rock Interaction. Springer, pp. 737–823.

Baldeyrou, A., Vidal, O., Fritz, B, 2003. Etude expérimentale des transformations de phase dans un gradient thermique: application au granite de Soultz-sous-Forêts, France. C. R. Geosci. 335, 371–380.

Bénézeth, P., Palmer, D.A., Wesolowski, D.J., 2001. Aqueous high temperature solubility studies. II. The solubility of boehmite at 0.03 ionic strength as a function of temperature and pH as determined by "in situ" measurements. Geochim.Cosmochim. Acta 65, 2097–2111.

Bénézeth, P., Palmer, D.A., Wesolowski, D.J., 2008. Dissolution/precipitation kinetics of boehmite and gibbsite: application of a pH-relaxation technique to study near-equilibrium rates. Geochim. Cosmochim. Acta 72, 2429–2453.

Bethke, C., 2008. Geochemical and Biogeochemical Reaction Modeling, 2nd edition. Cambridge University Press, p. 564.

Bickmore, B.R., Bosbach, D., Hochella Jr., M.F., Charlet, L., Rufe, E., 2001. In situ atomic force microscopy study of hectorite and nontronite dissolution: implications for phyllosilicate edge surface structures and dissolution mechanisms. Am. Mineral. 86, 411–423.

Bourcier, W.L., Knauss, K.G., Jackson, K.J., 1993. Aluminum hydrolysis constants to 250 C from boehmite solubility measurements. Geochim. Cosmochim. Acta 57, 747–762.

Bourg, A.C.M., Oustrière, P., Sureau, J.F., 1985. Experimental investigation of clogging of fissures and pores in granites. Mineral. Mag. 49, 223–231.

Brandt, F., Bosbach, D., Krawczyk-Bärsch, E., Arnold, T., Bernhard, G, 2003. Chlorite dissolution in the acid ph-range: a combined microscopic and macroscopic approach. Geochim. Cosmochim. Acta 67, 1451–1461.

Brantley, S.L., Mellott, N.P., 2000. Surface area and porosity of primary silicate minerals. Am. Mineral. 85, 1767–1783.

Charles, R.W., 1978. Experimental geothermal loop: I, 295 °C study. LA-7334-MS Informal Report. Los Alamos Scientific Laboratory, p. 44.

Cheng, Y., Zhang, Y., Yu, Z., Hu, Z., Yang, Y., 2020. An investigation on hydraulic fracturing characteristics in granite geothermal reservoir. Eng. Fract. Mech. 237, 107252.

Critelli, T., Marini, L., Schott, J., Mavromatis, V., Apollaro, C., et al., 2014. Dissolution rates of actinolite and chlorite from a whole-rock experimental study of metabasalt dissolution from 2≤pH≤12 at 25 °C. Chem. Geol. 390, 100–108.

Daval, D., Calvaruso, C., Guyot, F., Turpault, M.-.P., 2018. Time-dependent feldspar dissolution rates resulting from surface passivation: experimental evidence and geochemical implications. Earth Planet. Sci. Lett. 498, 226–236.

Daval, D., Hellmann, R., Saldi, G.D., Wirth, R., Knauss, K.G., 2013. Linking nm-scale measurements of the anisotropy of silicate surface reactivity to macroscopic dissolution rate laws: new insights based on diopside. Geochim. Cosmochim. Acta 107, 121–134.

Davatzes, N.C., Hickman, S.H., 2010. The feedback between stress, faulting, and fluid flow: lessons from the Coso Geothermal Field, CA, USA. In: *Proceedings World Geothermal Congress* 2010, Bali, Indonesia, Apr. 25–29, 2010, p. 15.

Dobson, P.F., Kneafsey, T.J., Nakagawa, S., Sonnenthal, E.L., Voltolini, M., et al., 2021. Fracture sustainability in enhanced geothermal systems: experimental and modeling constraints. J. Energy Resour. Technol. 143, 100901.

Duchane, D., Brown, D., 2002. Hot Dry Rock geothermal energy research and development at Fenton Hill, New Mexico. GHC Bulletin, pp. 13–19. *Dec. 2002*.

Edmunds, W.D., Kay, R.F.L., McCartney, R.A., 1985. Origin of saline groundwaters in the Carnmenellis granite (Cornwall, England): natural processes and reaction during hot dry rock reservoir circulation. Chem. Geol. 49, 287–301.

Entingh, D.J., 2000. Geothermal well stimulation experiments in the United States. In: Proceedings World Geothermal Congress 2000. Kyushu - Tohoku, Japan, pp. 3689–3694.

Farquharson, J.I., Kushnir, A.R.L., Wild, B., Baud, P., 2020. Physical property evolution of granite during experimental chemical stimulation. Geotherm. Energy 8 (14), 1–24. https://doi.org/10.1186/s40517-020-00168-7.

Fritz, B., Clément, A., Amal, Y., Noguera, C., 2009. Simulation of the nucleation and growth of simple clay minerals in weathering processes: the NANOKIN code. Geochim. Cosmochim. Acta 73, 1340–1358.

Fritz, B., Jacquot, E., Jacquemont, B., Baldeyrou-Bailly, R.M., Vidal, O, 2010. Geochemical modelling of fluid-rock interactions in the context of the Soultz-sous-Forêts geothermal system. C. R. Geosci. 342, 653–667.

Gallup, D.L., 1997. Aluminum silicate scale formation and inhibition: scale characterization and laboratory experiments. Geothermics 26, 483–499.

Ganor, J., Roueff, E., Erel, Y., Blum, J.D., 2005. Dissolution kinetics of a granite and its minerals—Implications for comparison between laboratory and field dissolution rates. Geochim. Cosmochim. Acta 69, 607–621.

Ganor, J., Lu, P., Zheng, Z., Zhu, C., 2007. Bridging the gap between laboratory measurements and field estimations of silicate weathering using simple calculations. Environ. Geol. 53, 599–610.

Gautier, J.-.M., 1999. Etude Expérimentale Et Modélisation De La Cinétique De Dissolution Et Cristallisation Des Silicates En Milieu hydrothermal: Cas Du Quartz Et Du Feldspath potassique. PhD Thesis. Université Paul Sabatier, Toulouse, p. 180.

Gautier, J.-M., Oelkers, E.H., Schott, J., 2001. Are quartz dissolution rates proportional to B.E.T. surface areas? Geochim. Cosmochim. Acta 65, 1059–1070.

Goddéris, Y., François, L.M., Probst, A., Schott, J., Moncoulon, D., et al., 2006. Modelling weathering processes at the catchment scale: the WITCH numerical model. Geochim. Cosmochim. Acta 70, 1128–1147.

Gunnarson, I., Arnórsson, 2003. Silica scaling: the main obstacle in efficient use of high-temperature geothermal fluids. In: International Geothermal Conference, Reykjavík, Sept. 2003, pp. 30–36. Session #13, paper 118.

Hellmann, R., 1994. The albite-water system: part I. The kinetics of dissolution as a function of pH at 100, 200 and 300 °C. Geochim. Cosmochim. Acta 58, 595–611.

Hellmann, R., Tisserand, D., 2006. Dissolution kinetics as a function of the Gibbs free energy of reaction: an experimental study based on albite feldspar. Geochim. Cosmochim. Acta 70, 364–383.

Heřmanská, M., Voigt, M.J., Marieni, C., Declercq, J., Oelkers, E.H., 2022. A comprehensive and internally consistent mineral dissolution rate database: part I: primary silicate minerals and glasses. Chem. Geol. 597, 120807.

Hodson, M.E., 1999. Micropore surface area variation with grain size in unweathered alkali feldspars: implications for surface roughness and dissolution studies. Geochim. Cosmochim. Acta 62, 3429–3435.

Komninou, A., Yardley, B.W.D., 1997. Fluid-rock interactions in the Rhine Graben: a thermodynamic model of the hydrothermal alteration observed in deep drilling. Geochim. Cosmochim. Acta 61, 515–531.

Lange, I., Toro, M., Arvidson, R.S., Kurganskaya, I., Luttge, A, 2021. The role of crystal heterogeneity in alkali feldspar dissolution kinetics. Geochim. Coscmochim. Acta 309, 329–351.

Lasaga, A., 1998. Transition State Theory. Kinetic Theory in the Earth Sciences. Princeton University Press, Princeton NJ, pp. 152–219.

Lo Ré, C., Kaszuba, J.P., Moore, J.N., McPherson, B.J., 2014. Fluid–rock interactions in CO2-saturated, granite-hosted geothermal systems: implications for natural and engineered systems from geochemical experiments and models. Geochim. Coscmochim. Acta 141, 160–178.

Lu, S.-M., 2018. A global review of enhanced geothermal system (EGS). Renew. Sustain. Energy Rev. 81, 2902–2921.

Lucas, Y., Ngo, V.V., Clément, A., Fritz, B., Schäfer, G., 2020. Modelling acid stimulation in the enhanced geothermal system of Soultz-sous-Forêts (Alsace, France). Geothermics 85, 101772.

Macht, F., Eusterhues, K., Pronk, G.J., Totsche, K.U., 2011. Specific surface area of clay minerals: comparison between atomic force microscopy measurements and bulk-gas (N$_2$) and -liquid (EGME) adsorption methods. Appl. Clay Sci. 53, 20–26.

Maher, K., Steefel, C.I., White, A.F., Stonestrom, D.A., 2009. The role of reaction affinity and secondary minerals in regulating chemical weathering rates at the Santa Cruz Soil Chronosequence, California. Geochim. Coscmochim. Acta 73, 2804–2831.

Maher, K., 2010. The dependence of chemical weathering rates on fluid residence time. Earth Planet Sci. Lett. 294, 101–110.

Marini, L., 2006. Geological Sequestration of Carbon Dioxide: Thermodynamics, Kinetics, and Reaction Path Modeling. Developments in Geochemistry, Developments in Geochemistry, 11. Elsevier, Amsterdam, p. 453.

McCartney, R.A., 1987. Hot dry rock geothermal systems: geochemical applications of transient field experiments. Geothermics 16, 419–428.

Meng, X., Liu, W., Meng, T, 2018. Experimental investigation of thermal cracking and permeability evolution of granite with varying initial damage under high temperature and triaxial compression. Adv. Mater. Sci. Eng. 2018, 87597401.

Moore, D.E., Lockner, D.A., Byerlee, J.D., 1994. Reduction of permeability in granite at elevated temperatures. Science 265, 1558–1561.

Nagy, K.L., Lasaga, A.C., 1992. Dissolution and precipitation kinetics of gibbsite at 80 °C and pH 3: the dependence on solution saturation state. Geochim. Cosmochim. Acta 56, 3093–3111.

Newton, C.J., Zarrouk, S.J., Lawless, J., Rowe, M.C., Guidos, J.A., Brown, K.L., 2018. Aluminium-rich silica scaling: san Jacinto-Tizate geothermal energy project, Nicaragua. In: Proceedings 40th New Zealand Geothermal Workshop 14-16 November 2018. Taupo, New Zealand.

Ngo, V.V., Lucas, Y., Clément, A., Fritz, B, 2016. Modeling the impact of temperature on the saturation state and behavior of minerals in the Soultz-sous-Forêts geothermal system. Geothermics 64, 196–208.

Nishimoto, S., Yoshida, H., 2010. Hydrothermal alteration of deep fractured granite: effects of dissolution and precipitation. Lithos 115, 153–162.

Nitschke, F., Scheiber, J., Kramar, U., Neumann, T., 2014. Formation of alternating layered Ba-Sr-sulfate and Pb-sulfide scaling in the geothermal plant of Soultz-sous-Forêts. N. Jb. Miner. Abh. (J. Min. Geochem.) 191, 145–156.

Noguera, C., Fritz, B., Clément, A., 2011. Simulation of the nucleation and growth of clay minerals coupled with cation exchange. Geochim. Cosmochim. Acta 75, 3402–3418.

Numakura, T., Watanabe, N., Sakaguchi, K., Kikuchi, T., Tsuchiya, N., 2015. Permeability measurements of fractured granite at 350-450 °C under confining stress. GRC Trans. 39, 329–334.

Palandri, J.L., Kharaka, Y.K., 2004. A compilation of rate parameters of water-mineral interaction kinetics for applications to geochemical modeling. U.S. Geological Survey Open File Report 2004-1068, p. 64.

Pan, F., McPherson, B., Lichtner, P., Kaszuba, J., Ré, Lo, et al., 2013. Numerical evaluation of energy extraction, CO2-rock interactions, and carbon sequestration in enhanced geothermal systems (EGS) with supercritical CO$_2$ as a working fluid. In: Proceedings, Thirty-Eighth Workshop on Geothermal Reservoir Engineering.

Paulillo, A., Striolo, A., Lettieri, P., 2019. The environmental impacts and the carbon intensity of geothermal energy: a case study on the Hellisheiði plant. Environ. Int. 133, 105226.

Pollet-Villard, M., Daval, D., Ackerer, P., Saldi, G.D., Wild, B., Knauss, K.G., Fritz, B., 2016. Does crystallographic anisotropy prevent the conventional treatment of aqueous mineral reactivity? A case study based on K-feldspar dissolution kinetics. Geochim. Cosmochim. Acta 190, 294–308.

Portier, S., Vuataz, F-D., 2010. Developing the ability to model acid-rock interactions and mineral dissolution during the RMA stimulation test performed at the Soultz-sous-Forêts EGS site, France. Comptes Rendus. Geosci. 342, 668–675.

Reed, M.J., 1989. Thermodynamic calculations of calcium carbonate scaling in geothermal wells, Dixie Valley geothermal field, U.S.A. Geothermics 18, 269–277.

Reinecker, J., Gutmanis, J., Foxford, A., Cotton, L., Dalby, C., 2021. Geothermal exploration and reservoir modelling of the united downs deep geothermal project, Cornwall (UK). Geothermics 97, 102226.

Richards, H.G., Savage, D., Andrews, J.N., 1992. Granite-water reactions in an experimental Hot Dry Rock geothermal reservoir, Rosemanowes test site, Cornwall, U. K. Appl. Geochem. 7, 193–222.

Rose, P., Xu, T., Kovac, K., Mella, M., Pruess, K., 2007. Chemical stimulation in near-wellbore geothermal formations: silica dissolution in the presence of calcite at high temperature and high pH. In: Proceedings of the thirty-second Workshop on Geothermal Reservoir Engineering, Stanford. California, 2007. University Stanford. January 22-24.

Rosener, M., Géraud, 2015. Using physical properties to understand the porosity network geometry evolution in gradually altered granites in damage zones. In: Rock Physics and Geomechanics in the Study of Reservoirs and Repositories, 284. Geological Society, London, pp. 175–184. Special Publications.

Saldi, G.D., Daval, D., Guo, H., Guyot, F., Bernard, S., et al., 2015. Mineralogical evolution of Fe–Si-rich layers at the olivine-water interface during carbonation reactions. Am. Mineral. 100, 2655–2669.

Sánchez-Roa, C., Saldi, G.D., Mitchell, T.M., Iacoviello, F., Bailey, J., Shearing, P.R., et al., 2021. The role of fluid chemistry on permeability evolution in granite: applications to natural and anthropogenic systems. Earth Planet. Sci. Lett. 553, 116641.

Savage, D., Cave, M., Milodowski, A.E., George, I., 1987. Hydrothermal alteration of granite by meteoric fluid: an example from the Carnmenellis Granite, United Kingdom. Contrib. Mineral. Petrol. 96, 391–405.

Savage, D., Soler, J.M., Yamaguchi, K., Walker, C., Honda, A., et al., 2011. A comparative study of the modelling of cement hydration and cement–rock laboratory experiments. Appl. Geochem. 26, 1138–1152.

Schill, E., Genter, A., Cuenot, Kohl, T, 2017. Hydraulic performance history at the Soultz EGS reservoirs from stimulation and long-term circulation tests. Geothermics 70, 110124.

Schott, J., Pokrovsky, O.S., Oelkers, E.H., 2009. The Link between mineral dissolution/precipitation kinetics and solution chemistry. Rev. Mineral. Geochem. 70, 207–258.

Schulz, K.E., Bär, K., Sass, I, 2022. Lab-scale permeability enhancement by chemical treatment in fractured granite (Cornubian Batholith) for the United Downs Deep Geothermal Power Project, Cornwall (UK). Geosciences (Basel) 12, 35.

Soler, J.P., Mäder, U.K., 2007. Mineralogical alteration and associated permeability changes induced by a high-pH plume: modeling of a granite core infiltration experiment. Appl. Geochem. 22, 17–29.

Stáhl, G., Pátzay, G., Weiser, L., Kálmán, E., 2000. Study of calcite scaling and corrosion processes in geothermal systems. Geothermics 29, 105–119.

Tester, J.W., Worley, W.G., Robinson, B.A., Grigsby, C.O., Feerer, J.L., 1994. Correlating quartz dissolution kinetics in pure water from 25 to 625 °C. Geochim. Cosmochim. Acta 58, 2407–2420.

Takaya, Y., 2014. Which constituent mineral is dominant in granite weathering? A solution-sided approach through a laboratory experiment. Geoderma 230-231, 204–211.

Tester, J.W., Anderson, B.J., Batchelor, A.S., Blackwell, D.D., DiPippo, R., et al., 2006. The future of geothermal energy: impact of enhanced geothermal systems (EGS) on the United States in the 21st century. An Assessment by an MIT-Led Interdisciplinary Panel, p. 372. Available at. https://www1.eere.energy.gov/geothermal/pdfs/future_geo_energy.pdf.

Velbel, M.A., 1993. Constancy of silicate-mineral weathering-rate ratios between natural and experimental weathering: implications for hydrologic control of differences in absolute rates. Chem. Geol. 105, 89–99.

Viani, B.E., Bruton, C.J., 1996. Effect of Cation Exchange of Major Cation Chemistry in the Large Scale Redox Experiment At Aspo. UCRL-JC-118592 Rev. 1 Preprint. Lawrence Livermore National Laboratory, p. 19.

Watanabe, N., Egawa, M., Sakaguchi, K., Ishibashi, T., Tsuchiya, N., 2017. Hydraulic fracturing and permeability enhancement in granite from subcritical/brittle to supercritical/ductile conditions. Geophys. Res. Lett. 44, 5468–5475.

Wesolowsky, D.J., Palmer, D.A., 1994. Aluminum speciation and equilibria in aqueous solution: V. Gibbsite solubility at 50°C and pH 3–9 in 0.1 molal NaCl solutions (a general model for aluminum speciation; analytical methods). Geochim. Cosmochim. Acta 58, 2947–2969.

White, A.F., 1995. Chemical Weathering rates of silicate minerals in soils. In: chemical weathering rates of silicate minerals. Rev. Mineral. 31, 407–462.

White, A.F., Brantley, S.L, 1995. Chemical weathering rates of silicate minerals. Rev. Mineral. 31, 583.

White, A.F., Brantley, S.L., 2003. The effect of time on the weathering of silicate minerals: why do weathering rates differ in the laboratory and field? Chem. Geol. 202, 479–506.

White, A.F., Peterson, M.L., et al., 1990. Role of reactive-surface-area characterization in geochemical kinetic models. In Chemical Modeling of Aqueous Systems II. In: Melchior, D., et al. (Eds.), ACS Symposium Series. American Chemical Society, Washington, DC, pp. 461–475. Chapter 35.

White, A.F., Schulz, M.S., Lawrence, C.R., Vivit, D.V., Stonestrom, D.A., 2017. Long-term flow-through column experiments and their relevance to natural granitoid weathering rates. Geochim. Cosmochim. Acta 202, 190–214.

Wild, B., Daval, D., Guyot, F., Knauss, K.G., et al., 2016. pH-dependent control of feldspar dissolution rate by altered surface layers. Chem. Geol. 442, 148–159.

Wild, B., Daval, D., Micha, J.-.B., Bourg, I.C., White, C.E., Fernandez-Martinez, A., 2019. Physical properties of interfacial layers developed on weathered silicates: a case study based on labradorite feldspar. J. Phys. Chem. C 123, 24520–24532.

Wilkin, R.T., Barnes, H.L., 2000. Nucleation and growth kinetics of analcime from precursor Na-clinoptilolite. Am. Mineral. 85, 1329–1341.

Wolery, T.J., 2010. In: EQ3/6: A Software Package for Geochemical Modeling. Computer Software. USDOE 13 Dec 2010. doi:10.11578/dc.20210416.44.

Wolery, T.W., Jarek, R.L., 2003. Software User's manual. EQ3/6, Version 8.0. U.S. Tech. Rep. Department of Energy, Office of Civilian Radioactive Waste Management, Office of Repository Development, 10813-UM-8.0-00.

Wolery, T.J., Jové Colón, C.F., 2017. Chemical thermodynamic data. 1. The concept of links to the chemical elements and the historical development of key thermodynamic data. Geochim. Cosmochim. Acta 213, 635–676.

Wu, L., Jacobson, A.D., Hausner, M., 2008. Characterization of elemental release during microbe–granite interactions at T=28°C. Geochim. Cosmochim. Acta 72, 1076–1095.

Xu, T., Spycher, N., Sonnenthal, E., Zhang, G., Zheng, L., 2011. TOUGHREACT Version 2.0: a simulator for subsurface reactive transport under non-isothermal multiphase flow conditions. Comput. Geosci. 37, 763–774.

Xu, T., Ontoy, Y., Molling, P., Spycher, N., Parini, M., Pruess, K., 2004. Reactive transport modeling of injection well scaling and acidizing at Tiwi field, Philippines. Geothermics 33, 477–491.

Yang, L., Steefel, C.I., 2008. Kaolinite dissolution and precipitation kinetics at 22 °C and pH 4. Geochim. Cosmochim. Acta 72, 99–116.

Yang, F., Yuan, K., Stack, A.G., Starchenko, V., 2022. Numerical study of mineral nucleation and growth on a substrate. ACS Earth Space Chem. 6, 1655–1665.

Yashuara, H., Kinoshita, N., Ohfuji, H., Lee, D.S., Nakashima, S., Kishida, K., 2011. Temporal alteration of fracture permeability in granite under hydrothermal conditions and its interpretation by coupled chemo-mechanical model. Appl. Geochem. 26, 2074–2088.